https://doi.org/10.5194/egusphere-2026-3456
Preprint. Discussion started: 1 July 2026


# The Max Planck CloudKite (MPCK): High-Resolution Airborne Measurements of Turbulence and Cloud Microphysics

Gholamhossein Bagheri[1], Freja Nordsiek[1], Oliver Schlenczek[1], Yewon Kim[1], Birte Thiede[1], Venecia Chávez-Medina[1], Philipp Höhne[1], Torben Neumann[1], and Eberhard Bodenschatz[1,2,3]

[1]Max Planck Institute for Dynamics and Self-Organization (MPI-DS), Am Faßberg 17, 37077 Göttingen, Germany
[2]Institute for Dynamics of Complex Systems, Georg-August University of Göttingen, Friedrich-Hund-Platz 1, 37077 Göttingen, Germany
[3]Laboratory of Atomic and Solid State Physics and Sibley School of Mechanical and Aerospace Engineering, Cornell University, 130 Upton Hall, Ithaca NY 14853, USA

**Correspondence:** Gholamhossein Bagheri (gholamhossein.bagheri@ds.mpg.de) and Eberhard Bodenschatz (eberhard.bodenschatz@ds.mpg.de)

**Abstract.** We present the airborne Max Planck CloudKite (MPCK) platform, an instrumented tethered aerostat for atmospheric and cloud research, together with its first dedicated measurement system, the Advanced Max Planck CloudKite (MPCK$^+$) instrument, designed for high-resolution observations of cloud microphysics and turbulence up to 2 km above ground level. The platform and instrument design are described, and their performance is evaluated through laboratory characterisation, wind-tunnel experiments, and multiple field campaigns over land and aboard research vessels. These evaluations also include assessments of mounting strategies and flight stability. The MPCK$^+$ instrument combines advanced airborne imaging techniques: in-line holography, which characterises particle size, concentration, and shape in three dimensions, and particle image velocimetry (PIV), implemented here for the first time in an in-situ airborne setting. Together, they enable co-located, high-cadence observations of cloud microphysics and turbulence. Intercomparisons with conventional probes (e.g. cloud droplet probes and pitot tubes) show consistent measurements of bulk quantities, while MPCK$^+$ uniquely provides spatially resolved, co-located particle and flow fields, enabling direct observation of localised cloud microphysics–turbulence interactions inaccessible to conventional non-imaging instrumentation. Field performance evaluations demonstrate robust measurements of droplet size, concentration, and turbulence properties across a wide range of cloud conditions. These results demonstrate that the MPCK platform and MPCK$^+$ instrument provide an advanced observational capability for studying cloud microphysics–turbulence interactions, bridging micrometre-scale resolution with continuous sampling over tens of kilometres.

## 1 Introduction

Clouds are fundamental to Earth's climate system, controlling its radiative and hydrological balance while remaining a major source of uncertainty in weather and climate models(Shaw, 2003; Bodenschatz et al., 2010; Morrison et al., 2012; Grabowski

https://doi.org/10.5194/egusphere-2026-3456
Preprint. Discussion started: 1 July 2026


and Wang, 2013; Korolev et al., 2017; Intergovernmental Panel on Climate Change, 2021). Constraining cloud dynamics in such models is challenging because the governing processes span an enormous range of scales, from nanometres, where aerosol activation and droplet formation occur, to hundreds of kilometres, where clouds are embedded within larger synoptic scales (Bodenschatz et al., 2010). At intermediate scales, from millimetres to hundreds of metres, interactions with intense turbulence drive key processes that control entrainment, mixing, and particle dynamics. These processes include droplet evaporation and condensational growth, as well as collision and coalescence or aggregation within clouds, and they ultimately determine cloud evolution and lifetime (see e.g. Shaw, 2003; Devenish et al., 2012; Grabowski and Wang, 2013; Pumir and Wilkinson, 2016, and references therein). Laboratory experiments and numerical simulations have provided valuable insights into cloud processes, yet they cannot fully reproduce the strength and scale range of atmospheric turbulence in natural clouds. Remote-sensing observations provide continuous coverage over large regions but cannot resolve small-scale cloud microphysics. Direct in-situ observations capable of capturing microphysics and turbulence at the relevant scales within clouds are therefore indispensable.

Standard in-situ methods include ground-based research stations, towers, airplanes, helicopters, Uncrewed Aerial Vehicles (UAVs), and balloons/aerostats (both free and tethered). Ground-based stations benefit from much less restrictive weight and power constraints than airborne platforms and can provide continuous measurements over periods from years to decades. However, their altitude reach is limited, typically to a few hundred metres above ground level using mountain stations, towers or masts, and they must wait for clouds to pass through while also contending with local topographic influences on cloud structure. To obtain in-situ measurements of higher altitude clouds, away from topographic influences, airborne platforms are required. Airborne platforms form a spectrum between fast platforms like airplanes that travel fast enough that Taylor's frozen field hypothesis reasonably applies to very low platform velocities relative to the air, like free balloons, where measurements are closer to Lagrangian and smaller spatial scales can be resolved for a given temporal sampling resolution.

Aircraft-based platforms offer the greatest flexibility for selecting clouds of interest, with the ability to carry heavy payloads and to cover large areas, although they are subject to operational constraints in conditions with icing potential. The high true air speed (TAS) of aircraft, typically 70–200 m/s, constrains in-situ turbulence measurements, as the spatial and temporal averaging scales must be long enough to obtain robust statistics yet short enough to capture inhomogeneities and turbulent structures of interest (Schröder et al., 2024). Studies using optical array probes have also been instrumental in advancing our understanding (e.g. see Baumgardner et al., 2017; McFarquhar et al., 2017, and references therein), including recent investigations of phase distributions in mixed-phase clouds down to spatial scales of about 100 m (Korolev and Milbrandt, 2022). However, the pseudo-one-dimensional sampling of these instruments, which requires averaging droplet statistics along the flight trajectory, significantly limits the ability to resolve small-scale cloud features below $\sim$100 m. Several previous studies have employed advanced holographic instruments aboard research aircraft to capture localised three-dimensional cloud volumes and characterise particle number, size, and shape distributions. These include investigations of droplet spatial distributions in cumulus clouds (Beals et al., 2015), large stratocumulus decks (Glienke et al., 2020), and variability in droplet size distributions (Allwayin et al., 2024), as well as studies of ice crystal environments, spatial distributions, and habits in cumulonimbus and ice clouds (Schlenczek, 2018). However, aircraft-based holographic measurements remain limited in spatial resolution, typically $\sim$30 m

https://doi.org/10.5194/egusphere-2026-3456
Preprint. Discussion started: 1 July 2026


between successive holograms, due to the high aircraft TAS and the relatively low acquisition rates of currently available aircraft-certified instruments.

Helicopters share many of aircraft advantages and can fly at a lower TAS of about 20 m/s (e.g. Muschinski et al., 2001; Siebert et al., 2006), enabling a significant improvement in spatial sampling resolution. However, they generally probe only the upper parts of clouds or cloud-free regions due restrictions imposed for flying helicopters inside clouds. Motorised UAVs, including multirotor drones and uncrewed fixed-wing aircraft, have recently gained popularity due to their rapid deployment, flexible flight strategies, and broad altitude range. Their main limitations remain the requirement to stay within visual line of sight in most regulated airspaces, which limits operation inside clouds, as well as their low payload capacity, short flight duration, and the aerodynamic disturbances generated by the platform itself. Nevertheless, regulations and UAV technology are evolving rapidly, and together with advances in miniaturised instruments, UAVs are strong candidates for the future of airborne measurements.

The other category of airborne platforms includes free balloons/aerostats and tethered kites/aerostats. Systematic atmospheric profiling using tethered platforms began in 1749, when Alexander Wilson and Thomas Melville in Edinburgh launched paper kites carrying thermometers (Balsley et al., 1998). E. Douglas Archibald later achieved in 1884 the first systematic wind profiles with kite-borne anemometers reaching over 400 m (Conover, 1990). By the late nineteenth century, kites supplied most lower-atmospheric data, as free balloons were difficult to recover. Consequently, kite-borne instruments dominated until the 1930s, when radiosondes and aircraft offered less labour-intensive alternatives (Balsley et al., 1998). Following the introduction of the Parseval–Sigsfeld kite balloon in 1893 and the revival of its scientific use in the 1980s by CIRES researchers (Balsley et al., 1992), aerostats have since been widely used for atmospheric observations in subsequent decades (e.g. Pisano et al., 1997; Siebert et al., 2003; Stith et al., 2018; Egerer et al., 2019; Lonardi et al., 2022, and refernces therein).

In recent years, tethered aerostats that combine helium buoyancy with aerodynamic lift have emerged as particularly attractive airborne platforms, as they can operate reliably in both calm and windy conditions and have been widely used to probe the atmosphere, aerosols, and clouds from tropical to polar regions(Krastel et al., 2019; Ramelli et al., 2020; Karstensen et al., 2020; Stevens et al., 2021; Zinke et al., 2021; Pasquier et al., 2022; Schröder, 2023; Pasquier et al., 2023; Henneberger et al., 2023; Ramelli et al., 2024; Schlenczek et al., 2025; Chávez-Medina et al., 2025; Thiede et al., 2025b, a; Fuchs et al., 2025; Creamean et al., 2025; Pohorsky et al., 2025). Such platforms also enable long-duration, nearly continuous measurements from hours to days, offer relatively large payload capacities from a few kilograms to several tens of kilograms, and avoid the high operational costs and certification requirements associated with aircraft and helicopters. Most importantly, they can operate freely inside clouds. Their tether functions as a kilometre-long tower for flexible placement of instruments at desired altitudes and, together with a winch system, allows controlled probing of atmospheric layers up to about typically 2 km above ground level. The Max Planck CloudKite (MPCK) platform introduced here employs a similar class of tethered aerostats, commercially known as HeliKites (Allsopp Helikites Ltd), which are hybrids of a kite and a helium-filled balloon with capacities ranging from 34 to 250 $m^3$. The MPCK primary aerostat is approximately 15 m long and 10 m high, with a helium volume of 250 $m^3$. It underwent its maiden test flight in March 2017 in Göttingen near the Max Planck Institute for Dynamics and Self-Organisation (MPI-DS), can lift about 100 kg of net payload using buoyancy alone, and has been operated reliably in winds up to $\sim$25 m/s.

https://doi.org/10.5194/egusphere-2026-3456
Preprint. Discussion started: 1 July 2026


Prior to the development of the MPCK project, which began in early 2016, imaging technologies developed had advanced beyond traditional optical array probes to include holographic systems such as HOLODEC (Fugal and Shaw, 2009a), PHIPS-HALO (Abdelmonem et al., 2016), and HALOHolo (Schlenczek, 2018), as well as the video ice particle sampler (VIPS) (Heymsfield and McFarquhar, 1996), among others. These instruments significantly improved particle detection and sizing, but challenges remain in capturing the coupling between turbulence and microphysics at sub-metre scales. In particular, turbulence characterisation has so far relied on conventional anemometry, which cannot resolve instantaneous flow structures at the relevant spatial and temporal scales (Schröder et al., 2024).

The goal of developing an instrument for the MPCK platform was to employ advanced imaging systems to resolve fine-scale cloud microphysics and their interaction with local turbulence. To achieve this, we have designed the Advanced Max Planck CloudKite (MPCK$^+$) instrument, which, to the authors' best knowledge, incorporates the fastest airborne holographic system together with the first airborne particle image velocimetry (PIV) system, capable of providing instantaneous statistics on cloud microphysics and turbulence-related quantities. These advanced imaging modules are complemented by conventional instruments for measuring wind velocity, droplet size distributions, and thermodynamic-state variables of the air. The MPCK$^+$ (including radio links and battery) forms an instrument roughly 1 m long/wide and 0.6 m high with a total weight of about 80 kg. The MPCK platform and the MPCK$^+$ have already been partially described by Höhne (2019); Schröder (2023); Thiede et al. (2025a); Schlenczek et al. (2025); Chávez-Medina et al. (2025), and briefly in the cruise reports (Krastel et al., 2019; Karstensen et al., 2020) and also by Stevens et al. (2021). However, a self-contained and thorough description of the MPCK platform and the MPCK$^+$ instrument, including detailed specifications, analysis methods, calibration strategies, and evaluations of data quality and measurement performance, has not yet been presented and is the primary aim of this manuscript. Other instruments have also been developed for the MPCK platform, including the mini-MPCK (Schröder, 2023), the WinDarts (Chávez-Medina et al., 2025), and the HoloTrack (Thiede et al., 2025b), but are not discussed further in this manuscript.

In the following sections, we first describe the MPCK platform (Sec. 2), including the aerostat, flight operations, and mounting strategies, followed by the advanced Max Planck CloudKite (MPCK$^+$) instrument (Sec. 3), with emphasis on its particle imaging systems. Then MPCK$^+$ performance, validity, and reliability are evaluated using data recorded in the laboratory and during field campaigns (Sec. 7). The results presented here characterise the strengths and limitations of measurements obtained with the MPCK systems and provide a primary reference for future publications based on these systems. They also offer practical guidance for the design, the deployment of tethered aerostat platforms and payload mounting strategies drawing on real-world experience from multiple field campaigns.

## 2 The MPCK platform

The MPCK platform is a tethered, lighter-than-air airborne system designed for high-resolution measurements of clouds and turbulence at altitudes up to 2 km above ground level (AGL). It consists of four main components: (i) the Helikite aerostat, (ii) a winch for altitude control, (iii) the tether, and (iv) ground-based infrastructure for operations and monitoring (Fig. 1). In the

https://doi.org/10.5194/egusphere-2026-3456
Preprint. Discussion started: 1 July 2026


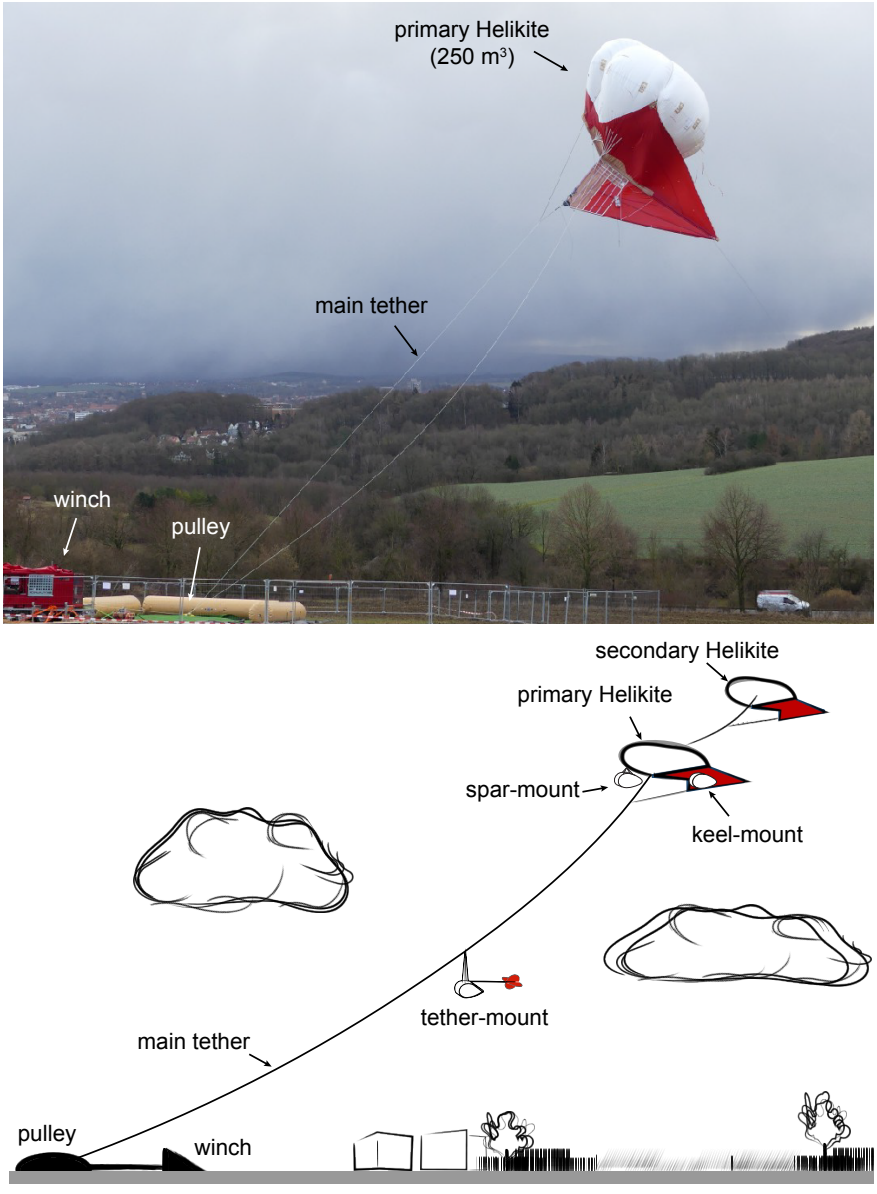


**Figure 1.** Overview of the MPCK platform and its main components. **Top:** Photograph of the primary 250 $m^3$ aerostat, the main tether, winch, and pulley system during a test flight near the Max Planck Institute for Dynamics and Self-Organization, Göttingen (Germany), in 2019. The second (backup) tether visible in this photo is used only during test flights for safety; during regular operations, only the main tether is connected to the aerostat. **Bottom:** Schematic of the tandem aerostat configuration and various instrument mounting positions of $MPCK^+$, i.e. spar-mount, keel-mount and tether-mount. For the tether-mounted configuration, the $MPCK^+$ instrument is equipped with a wind-stabilising tail. The schematic is not to scale.

https://doi.org/10.5194/egusphere-2026-3456
Preprint. Discussion started: 1 July 2026


following, we describe the main components of the MPCK platform and discuss key operational considerations, including the mounting strategies developed for different measurement configurations.

### 2.1 MPCK Aerostat

The MPCK platform uses a 250 $m^3$ Desert Star Helikite (Allsopp Helikites Ltd) as its primary aerostat. Helikites combine helium buoyancy with aerodynamic lift generated its kite, composed of a keel and sail, enabling stable flight even in strong winds of up to 25 m/s (depending on the model). The keel aligns the balloon with the wind, while the sail provides additional lift in windy conditions. This design allows stable operation at a typical tilt angle of about 40-55° from vertical, maintaining tether tension and platform stability. The primary aerostat is about 15 m long, 10 m wide/high and constructed with a polyurethane inner bladder and a ripstop nylon outer shell for strength.

To increase payload capacity under low-wind conditions, the MPCK can be operated in a tandem configuration, where a secondary Helikite (34–250 $m^3$) is stacked 50–100 m above the primary balloon. This configuration increases net helium buoyancy by about 10-50 kg (depending on the size of the tandem aerostat) while improving stability during flight. The aerodynamic lift generated by the HeliKite in strong winds can far exceed the static helium buoyancy. For example, for the primary 250 $m^3$ MPCK aerostat operating in tandem with a 34 $m^3$ Helikite, we have measured tether line tensions exceeding 1000 kg at wind speeds of about 25 m/s.

### 2.2 Winch and Tether System

The Helikite is tethered to the ground by a 2–4 km made of ultra-high-molecular-weight polyethylene (e.g. Dyneema or equivalent) tether and controlled using a petrol or a diesel powered winch. The main winch is capable of maintaining several tons of line tension and operates at reeling speeds up to 200 m/min, enabling rapid ascent and descent. A smaller handling winch, powered by a car battery, is also used during take-off and landing to provide fine control of the aerostat altitude near the ground (up to ∼50 m AGL), where winds are weaker. The aerostat altitude during measurements is adjusted by winching the tether in or out, with flight levels decided by buoyancy, tether length, wind-speed, payload weight and local airspace restrictions. Typical flight heights range between 0.5 km and 2.0 km.

### 2.3 Mounting Configurations

The scientific payloads can be mounted in three ways: (i) *keel-mount*, positioned a 3-5 meters below the helium-balloon along the keel; (ii) *spar-mount*, suspended directly (0.5 m) beneath the helium-balloon on short lines for rapid exchange of instruments; or (iii) *tether-mount*, attached along the main tether at variable distances below the balloon, which can minimise aerodynamic interference when feasible. The choice depends on operational constraints, payload size, and required measurement conditions. The tether mount, in particular, enables highly flexible deployment strategies that effectively transform the MPCK platform into a mobile, kilometre-high instrumented tower capable of making simultaneous measurements at multiple, arbitrarily chosen altitudes.

https://doi.org/10.5194/egusphere-2026-3456
Preprint. Discussion started: 1 July 2026


### 2.4 Flight Operation

Flights typically reach altitudes of up to 2 km AGL within 15–30 minutes. Altitude is controlled through controlled ascent/descent or staircase profiles to match cloud levels. Laser-based instruments are operated only above a prescribed altitude threshold, typically 400 m AGL, for laser-safety reasons, even though the MPCK$^+$ instrument is classified as Class 1 at a (conservative) distance of 30 m. Imaging instruments are activated only in cloud to conserve power and data storage. Cloud presence, for triggering holography and PIV imaging systems, is detected primarily by a cloud droplet probe running continuously above the laser safety altitude, with relative humidity measurements used as a fallback. For safety, operations are conducted in restricted airspace with ADS-B monitoring for aircraft. A field mill continuously monitors electric fields; operations are suspended if values exceed 500 V/m to reduce lightning risk.

## 3 The Advanced Max Planck CloudKite Instrument (MPCK$^+$)

The central goal in developing the MPCK$^+$ instrument is to link instantaneous cloud features (e.g., droplet number, size, and concentration) with the local turbulence, primarily through two in-house–developed imaging instruments: (i) a fast inline holographic module operating at 75 Hz with an effective pixel size of 3 µm and a sampling volume of about 50 mL; and (ii) a PIV system operating at 15 Hz with an effective pixel size of 100 µm and a sampling volume of about 45 mL. In particular, the use of advanced imaging systems allows localized estimation of cloud microphysical and turbulent properties without relying on assumptions commonly required by conventional anemometers or scattering probes, such as Taylor's frozen-turbulence hypothesis or the spherical shape of sampled particles. Combined with the low TAS of the MPCK platform, high-speed direct imaging enables localised, high-cadence measurements of key parameters, providing a means to investigate entrainment and mixing processes, droplet spatial structure and size distributions, and the evolution of liquid water content and turbulence from the cloud edge to the core.

Many established instruments commonly used in cloud research count and size particles within small view volumes — e.g., Cloud Droplet Probes (CDP), Cloud Particle Imagers (CPI/CIP), and Backscatter Cloud Probes (BCP) (Korolev et al., 2017). Laser Doppler Velocimetry/Anemometry (LDV/LDA) provides particle counts and a single velocity component, while Phase Doppler Interferometry (PDI) adds sizing. However, these swept-volume methods are quasi–one-dimensional (the 1D radial distribution differs fundamentally from the 3D case (Holtzer and Collins, 2002; Larsen et al., 2014)), have small cross sections that limit volumetric sampling at low airspeeds, and typically rely on Taylor's frozen-field hypothesis for droplet clustering and structure-function analyses. Consequently, they require substantial averaging — often over $\mathcal{O}(10^2)$ m on fast aircraft — thereby obscuring fine-scale cloud–turbulence structure. A CDP is nevertheless included in the MPCK$^+$ instrument to provide triggering for the imaging systems, as well as redundancy, verification, and fault diagnosis.

Considering cloud microphysics alone, inline holography addresses many limitations of above-mentioned instruments by capturing large three-dimensional particle fields in a single snapshot (Fugal and Shaw, 2009b; Henneberger et al., 2013; Ramelli et al., 2020; Glienke et al., 2020; Thiede et al., 2025c, b). To characterize turbulence, the MPCK$^+$ instrument is additionally equipped with (to the best of our knowledge) the first airborne 2D PIV system, enabling co-located particle size–position and

https://doi.org/10.5194/egusphere-2026-3456
Preprint. Discussion started: 1 July 2026


velocity measurements. This configuration enables direct estimation of the instantaneous turbulence energy dissipation rate — a key parameter that cannot be reliably derived from one-dimensional velocity records (Schröder et al., 2024) unless long averaging times in statistically stationary and homogeneous turbulence are assumed. This is a questionable assumption when applied to clouds, where cloud microphysical and turbulent properties may vary substantially in space.

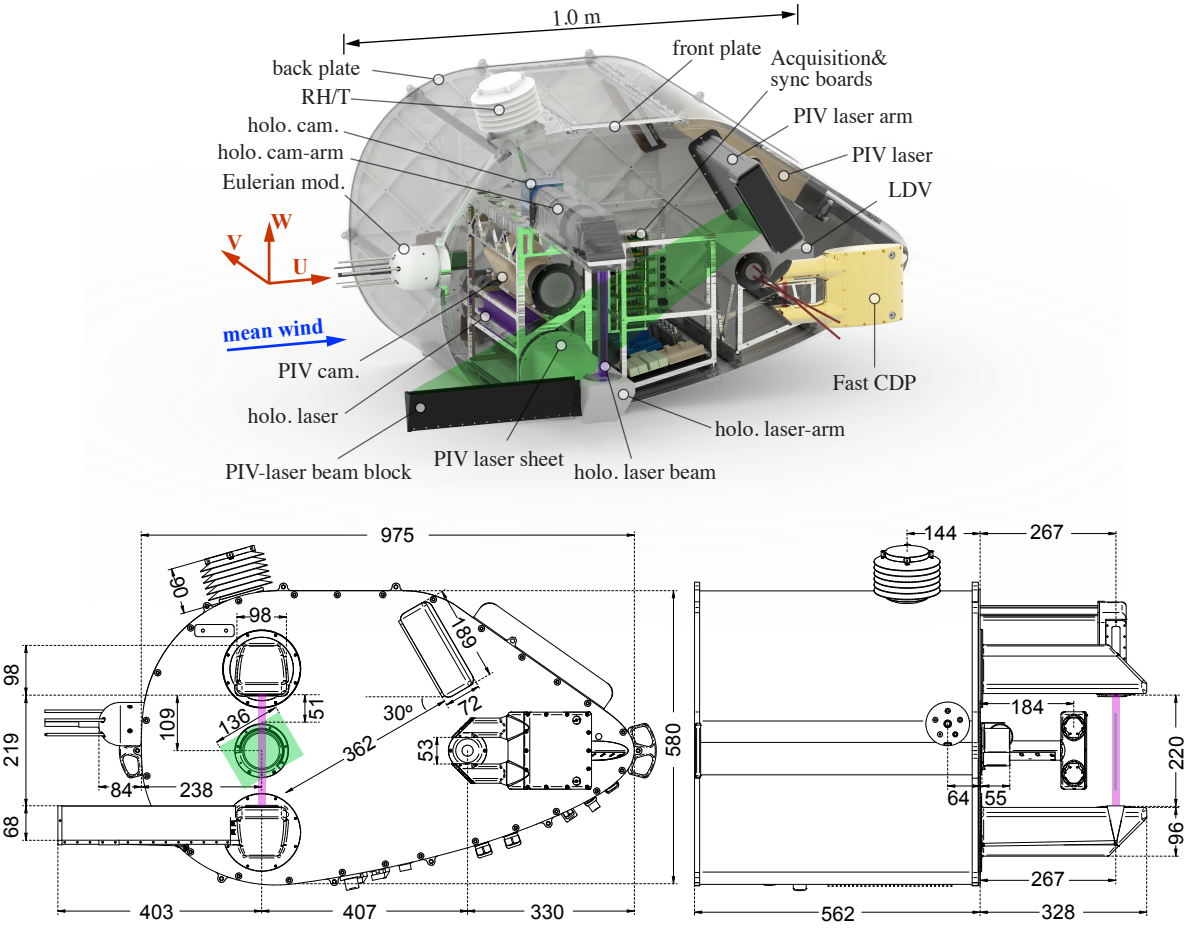


**Figure 2.** (Top) The MPCK$^+$ instrument and major subsystems. The vertical holography volume (purple) intersects the inclined PIV sheet (green), providing a co-located region for simultaneous characterisation of cloud microphysics and turbulence. The expected mean wind direction is indicated by the blue arrow entering near the Eulerian module, passing through the holographic and PIV sample volumes, and exiting at the right end near the Fast CDP. $U$ for the 1D and 3D pitot tubes, and $V$ and $W$ for the 3D pitot tube, indicate the directions of the longitudinal, lateral, and vertical wind velocity components, respectively. (bottom) MPCK$^+$ instrument drawings with the PIV and holography sampling regions shown in green and purple colours, respectively.

The MPCK$^+$ instrument integrates six subsystems: (i) *Particle Imaging* (inline holography + two-frame 2D PIV) with partially overlapping sample volumes; (ii) *Swept-Particle* (CDP) for low-power, continuous sizing; (iii) *Eulerian* (e.g. Pitot tubes

https://doi.org/10.5194/egusphere-2026-3456
Preprint. Discussion started: 1 July 2026


and cold/hot-wire) for local flow/thermodynamics; (iv) *Humidity*; (v) *Navigation* (GNSS/INS); and (vi) *Diagnostic video*. The MPCK$^+$ instrument is battery powered and can operate autonomously, switching the imaging systems on or off based on safety considerations (e.g. altitude) and preset triggers (e.g., inside or outside clouds with specific drop size/concentration features). The system can be monitored and controlled via multiple radio links operating at different frequencies, while all data are stored locally and downloaded after landing via ethernet and fibre-optic connections. It is certified as a class 1 laser system at a distance of 30 m due to integrated laser safety features, despite using class 4 lasers. Figure 2 shows the main components of the MPCK$^+$ instrument and Table 1 list all the major measurement components during the first two field campaign of the MPCK platforms. The layout prioritises overlapping sampling volumes between particle imaging systems and streamwise instrument alignment, enabling successive re-sampling of the same air or cloud parcel as it advects through the probing volumes of different instruments as much as possible. The holographic arms were modified in 2022 to improve their aerodynamic design and reduce disturbances to the airflow. The MPCK$^+$ instrument, including onboard computing, power distribution, laser safety systems, communication units, and a 10 kg, 1 kWh LiPo battery, has a total mass of approximately 80 kg.

**Table 1.** Instruments of the MPCK$^+$ instrument by system and, as an example, their operation during the first two field campaigns of the MPCK platform. Optical sampling rates are volumetric; for swept-volume instruments, TAS is the true airspeed and alignment with the wind is assumed. A blank campaign cell indicates "not used"; ✓ indicates success. Notes: [(1)] Communications and control problems; [(2)] Power box DC stage overheated; [(3)] Full sampling volume rate; [(4)] Data could not be downloaded; [(5)] GNSS reception issues; [(6)] GPS week roll-over handling failed; [(7)] Data corruption; [(8)] Could not connect; cause unknown.

| System | Kind | Model | Sampling Rate | MSM82/2 | MSM89 |
|---|---|---|---|---|---|
| Particle Imaging | PIV | custom | 0.670 L/s | failed[(1),(2)] | ✓ |
| | inline holography | custom | 3.88 L/s[(3)] | failed[(1),(2)] | ✓ |
| Swept Particle | CDP | SPEC Inc. FCDP | TAS · 0.325 mm$^2$ | marginal[(2)] | ✓ |
| | LDV | MSE miniLDV-G5 custom | TAS · 0.236 mm$^2$ | marginal[(4)] | |
| Eulerian | 1D pitot | Simtec/Swiss-Airdata PSS8 and HPS-1 | | ✓ | ✓ |
| | 3D pitot | Vectoflow S_5HP_ye1rjh + SVMtec PSC-5 | | ✓ | ✓ |
| | hotwire | Dantec 55P16 hotwire + 54T42 MiniCTA | | ✓ | ✓ |
| Humidity | fast RHT | UPSI F-TUTN.43 | | fragile | broke |
| | robust RHT | 1 or 2 Aosong AM2315 | | ✓ | ✓ |
| Navigation | INS | SBG Ellipse-N | | problems[(5)] | |
| | INS | SBG Ellipse2-D | | | problems[(5)] |
| | backup GNSS | Garmin GPS 15xH | | problems[(6)] | |
| | backup GNSS | ublox NEO-M8U | | | problems[(5),(7)] |
| Diagnostic Video | flight camera | Putal PTC08 (with waterproof housing) | | ✓ | ✓ |
| | interior camera | Putal PTC06 | | ✓ | failed[(8)] |

The inline holography runs at 75 Hz with $\sim 3$ µm effective pixel size and a snapshot volume $\mathcal{O}(50)$ cm$^3$. The 2D PIV operates at 15 Hz with a thin laser sheet (4 mm) aligned to the flow, effective pixel size $\sim 10^2$ µm, and illuminated volume

https://doi.org/10.5194/egusphere-2026-3456
Preprint. Discussion started: 1 July 2026


$\mathcal{O}(50)$ cm$^3$. Their overlap (about 7 cm$^3$) yields co-located size–velocity statistics and internal cross-checks; the non-overlap extends particle and velocity statistics for clustering and structure functions.

Expressed in Kolmogorov units across typical cloud dissipation rates $\langle\varepsilon\rangle = 10^{-4}$–$10^{-1}$ W/kg (with $\eta \approx 2.4$–$0.43$ mm, where $\eta$ is the Kolmogorov length scale), the holography volume spans roughly 6–36 $\eta$ by 6–36 $\eta$ laterally and 90–510 $\eta$ axially. The PIV light sheet spans about 56–315 $\eta$ by 40–225 $\eta$ with a thickness of 1.7–9.3 $\eta$, while the co-located overlap covers approximately 46–260 $\eta$ by 6–36 $\eta$ with the same 1.7–9.3 $\eta$ thickness. With effective pixel sizes of 3 µm (holography) and 100 µm (PIV), sub-Kolmogorov scales are resolved for $\langle\varepsilon\rangle \lesssim 10^{-1}$ W/kg ($\eta \approx 430$ µm), and at least one axis of each volume reaches into the inertial range except at the very lowest dissipation rates ($\sim 10^{-4}$ W/kg).

## 4 MPCK$^+$: Particle Imaging System

The MPCK$^+$ particle imaging system consists of an in-line holography and a two-frame PIV subsystem. Holography runs at 75 Hz and PIV at 15 Hz. This cadence yields closely spaced holograms while PIV pairs provide instantaneous two-component velocities. The overlapping PIV and holography sampling volumes and a synchronized timing such that every fifth hologram coincides with the first PIV image of each pair, provide crucial joint size and velocity information (see timing digrams shown in Figure S6). In the following section, the imaging systems and their respective specifications are described in detail.

### 4.1 The Inline Holography system

Holography enables reconstruction of a measurement volume by numerically propagating the recorded diffraction pattern to different axial planes, producing computationally refocused, depth-resolved three-dimensional images slice by slice (Fugal et al., 2009). In the reconstructed volume, objects can only be resolved and distinguished from noise if they are at least two pixels across. Though once an object is identified, features as small as a pixel on it can be found. The MPCK$^+$ inline holography system uses a 25 Mpx monochrome sensor (SVS-VISTEK HR25000MCX using Onsemi PYTHON25K sensor, 5120×5120 8-bit images, 4.5 µm pixel size) with 1.5× magnification through a bi-telecentric lens (TDL65/1.5 UV S5LPJ2755, Sill Optics, custom-designed for MPCK$^+$), giving an effective pixel size of 3 µm, and a 355 nm near-UV pulsed laser (Crylas GmbH, pulse duration about 1.1 ns). Although the in-house MPCK$^+$ acquisition code has been tested and verified to operate the holography camera at 80 Hz, it is deliberately run at 75 Hz so that every fifth hologram coincides with a PIV image pair acquired at 15 Hz. Other design choices, e.g. arm orientation and separation, followed from these parameters and mechanical considerations. A collimated holographic beam was used for simplicity in optical design and processing, following Spuler and Fugal (2011).

The holographic sample volume is constrained by the effective image plane (1.54 cm × 1.54 cm) and the distance between the two arms of 22 cm (leading to a total sampling volume of 52 cm$^3$), although in practice a reduced sub-volume is usually used (usually between 4-18 cm away from the camera window below the top arm) to neglect the effect of the instrument arms. Theoretically, the resulting effective pixel size of 3 µm allows the detection of particles nominally down to 6 µm in diameter up to a depth distance of about $z = 13$ cm from the image plane located at the window of the top arm (see Figure 3(a)). At larger distances, this limit increases to about 12 µm in diameter at $z = 22$ cm. These theoretical limits and their verifications

https://doi.org/10.5194/egusphere-2026-3456
Preprint. Discussion started: 1 July 2026


for the MPCK$^+$ holographic system are detailed in the supplement Section 1.1. Thiede et al. (2025c) provides a thorough experimental quantification of the performance of the MPCK$^+$ holographic system and improved processing methods for analysing holograms. Here, we present additional performance assessments that complement and extend that work.

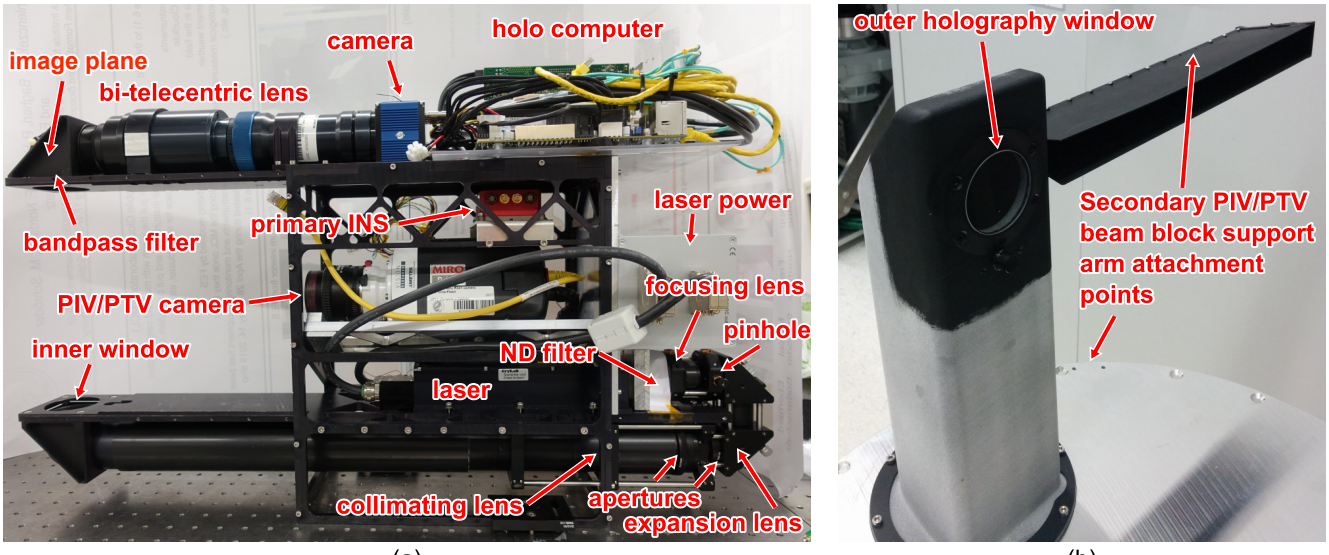


**Figure 3.** (a) Picture of the removed holography and PIV structure in the same configuration as for EUREC$^4$A with labels for the optical components. (b) The cover for the lower holographic arm (first version before 2022) with the attached PIV laser-beam block. The attachment points for the secondary support of the PIV beam block and the outer holography window are labelled. Holographic arm covers were modified in 2022 to improve aerodynamics and reduce disturbances between the holographic arms.

The optical system follows a standard inline holography setup: pulsed laser, neutral density (ND) filter, spatial filter, beam expansion and collimation with apertures, exit window from the laser side, entrance window on the camera side, bandpass filter, bi-telecentric objective lens, and camera (similar to e.g. HOLODEC II (Beals, 2013) and HALOHolo (Schlenczek, 2018)). The optics run in straight segments with 90° turns on the front removable frame of the MPCK$^+$ (Fig. 3) with freedom to move the beam expansion and collimating optics forward and backwards along the optical path to adjust the beam expansion and collimation. The outer protective covers of the holography arms are 3D printed from Nylon 12 and are mounted on the outside of the front plate after the MPCK$^+$ housing is closed (see Fig. 3b). Each cover is attached only at its base to the front plate so that aerodynamic loads on the covers are mechanically decoupled from the frame of imaging systems. Holographic laser-side components are on the bottom arm and camera-side components on the top arm to mitigate window contamination near the image plane since camera-side particles form sharp images that obscure targets, whereas laser-side particles produce diffuse diffraction with less impact.

Due to space constraints on the laser side, the optics are folded: the laser and spatial filter sit on top of the arm, pointing away from the holography sampling volume; two turning mirrors redirect the beam to the opposite side toward the view volume;

https://doi.org/10.5194/egusphere-2026-3456
Preprint. Discussion started: 1 July 2026


the expansion and collimating lenses and apertures are mounted underneath (see Fig. 3a and Fig. S7 in the Supplementary Material). Optical cage and lens tube systems (see Figure S7) are used for the laser side optics to hold and align the optics, block dust and stray light and make the optical more resistant to vibration.

We use a 355 nm pulsed laser with an energy of about 70 µJ and a pulse duration of 1.1 ns, operating at repetition rates up to 100 Hz, which covers the maximum camera frame rate of 80 fps. Even at TAS up to 100 m/s, particles move only a fraction of a pixel during illumination, so the measurements can be regarded as effectively instantaneous. The pulse energy is chosen to remain sufficient as the laser ages. Initially, a neutral-density filter attenuates the beam so that the hologram background is about 70% of the camera pixel well depth, and progressively weaker filters can be used as the laser output decreases. After the ND filter, the beam is spatially filtered to produce a clean Gaussian profile. Because the pulse energy is too high for a single-mode fibre, we use a lens–pinhole spatial filter comprising an 8 mm focal-length aspheric lens (Thorlabs A240TM-A) and a 15 µm diamond pinhole (Lenox Laser HEA-15D-R) mounted in XY and XYZ translation stages for precise alignment. The beam is then over-expanded and clipped by an aperture, to flatten its profile and minimise background non-uniformity, and finally collimated with a lens. Mirrors in the lower arm direct the collimated beam through a sapphire window into the sample volume and then into the upper arm. There, the light passes an OD4 band-pass filter and the bi-telecentric lens, with 1.5×magnification, a working distance of 105 mm, a numerical aperture of 0.13, and a transmission efficiency of about 70 %. The lens provides a mean modulation transfer function above 40 % at 160 lp/mm (≈3.1 µm), after which the magnified hologram is recorded by the camera sensor. The 355 nm source poses eye/skin hazards, but although 20% reflects from the uncoated sapphire window, multiple reflections and absorption by black surfaces reduce stray light to eye/skin-safe levels at 15 m for a 100 s exposure.

We used a compact Supermicro X10SDV-4C-7TP4F (Intel Xeon D-1518, 16 GB RAM) system with dual PCIe 3.0 ×8 slots to support high-rate, continuous image acquisition and storage until the available disk capacity is reached. Holograms were written to two NVMe SSDs in RAID 0 to avoid thermal throttling and sustain the required data rate. The initial configuration (prior to 2026) provided ∼4 TB of storage (156270 holograms), enabling ∼35 min of continuous acquisition per flight. This corresponds to sampled volumes of ∼4.8–8.1 $m^3$ for 6–10 µm particles and, at a wind speed of 10 $m\,s^{-1}$, a spatial coverage exceeding 20 km. The storage capacity has recently been upgraded to 16 TB, enabling up to 140 min of continuous acquisition per flight, corresponding to a continuous sampling distance of ∼80 km at a hologram spacing of ∼13 cm (for a true airspeed of 10 $m\,s^{-1}$). To reduce power usage, the holography camera is run by a dedicated computer (see Figure S9) that is turned off when not in use. The timing diagrams of the holography and PIV subsystems are discussed in more detail in the following section (see also Fig. S6).

#### 4.1.1 Particle Detection & Sizing Performance

The MPCK$^+$ holography setup was fully calibrated before its first field campaign in 2019 (MSM82/2), as shown below. However, in the meantime we extensively verified the performance of in-line holography using the MPCK$^+$ instrument and an optimized processing in separate study (Thiede et al., 2025c). This verification included comprehensive laboratory evaluations and in-situ measurements from the EUREC$^4$A campaign, as well as the development of a convolutional neural network (CNN) for particle classification. Comprehensive investigation of Thiede et al. (2025c) found that for holograms obtained with the

https://doi.org/10.5194/egusphere-2026-3456
Preprint. Discussion started: 1 July 2026


MPCK$^+$, the CNN achieves over 90% recall and precision for particles larger than 7 µm in a $10 \times 1.3 \times 1.3\,\mathrm{cm}^3$ detection volume. The average axial position error (along camera axis) remains below 150 µm (approximately 1.5 times the reconstruction resolution) for particles within 10 cm of the image plane. In-plane random position-errors stay below five pixels (mean $< 2$ pixels). A sizing error with standard deviation to about 2 µm was also achieved with a tuned sizing. Therefore, we believe that the performance of the MPCK$^+$ holographic setup is already thoroughly assessed by Thiede et al. (2025c) and has been demonstrated to match the expected performance. Nevertheless, for the sake of completeness, we provide below a brief report on the calibrations we performed prior to the publication of Thiede et al. (2025c).

We have evaluated sizing accuracy for spherical droplets by dispensing known-diameter glass microspheres (8–50 µm nominal diameters) into the holographic volume. Particles were introduced by tapping them from a container cap above the measurement region. The holograms were reconstructed with HoloSuite but sizing was performed with a sphere-specific sign-match filter approach that is threshold independent and therefore shows only pure instrument sizing errors (Lu et al., 2012). The results are compared to manufacturer specified mean diameters and measurements with an established holographic instrument HALOHolo (see e.g. Schlenczek, 2018). Fig. 4 show that the measurements agree well with manufacturer-specified mean diameters though they exceed HALOHolo-based measurements by up to 3 µm. This offset is comparable to the effective pixel size ($\approx 3$ µm) and is not statistically significant in most cases.

However, near the diffraction limit (see supplementary material 1.1), caution is needed; for 10 µm particles, the cumulative distribution function (CDF) suggests an effective pixel-size shift beyond the diffraction limit. For most measurements, due to computational limits a faster pixel-thresholding method is applied to size particles. This method can have higher uncertainty in measured diameters (Lu et al., 2012) as it depends on the chosen threshold. However, we have recently tuned the threshold-based sizing method with a combined approach and achieved a standard deviation of less than 2 µm over a wide range of sizes with the MPCK$^+$ holography setup (Thiede et al., 2025c).

To assess shape characterization performance of the setup, critical for distinguishing ice and mixed-phase particles, we designed a custom calibration mask featuring a grid of eight shapes and six sizes (20–200 µm circumscribed diameters), spaced 1 mm apart. The shapes included a triangle, square, six-pointed star, hexagon, circle, plus, minus, and the letter 'U'. These were 3D-printed onto a microscope slide using a Nanoscribe GT printer with <1 µm lateral precision in UV-absorbing IP-S resin.

In Figure 5, holograms were recorded using the full system, with the outer covers of the arms removed to compensate for the brightness reduction caused by the calibration-mask-substrate, and reconstructed with Holo Suite. At small $z$ (0.94 cm), all shapes were distinguishable, except for the 20 µm circle and hexagon. At large $z$ (23.51 cm), diffraction reduced contrast, making 20 µm targets barely visible and 40 µm targets only marginally distinguishable. All larger shapes remained clearly identifiable.

### 4.2 2-Frame Particle Image Velocimetry (PIV) System

To resolve instantaneous velocity gradients and estimate turbulence energy dissipation within clouds, the MPCK$^+$ instrument incorporates a compact two-frame PIV system. Unlike pitot-based methods that require long averaging windows, e.g. pitot tubes or ultrasonic anemometers, two-frame PIV provides direct, snapshot-based velocity gradients suitable for intermittent

https://doi.org/10.5194/egusphere-2026-3456
Preprint. Discussion started: 1 July 2026


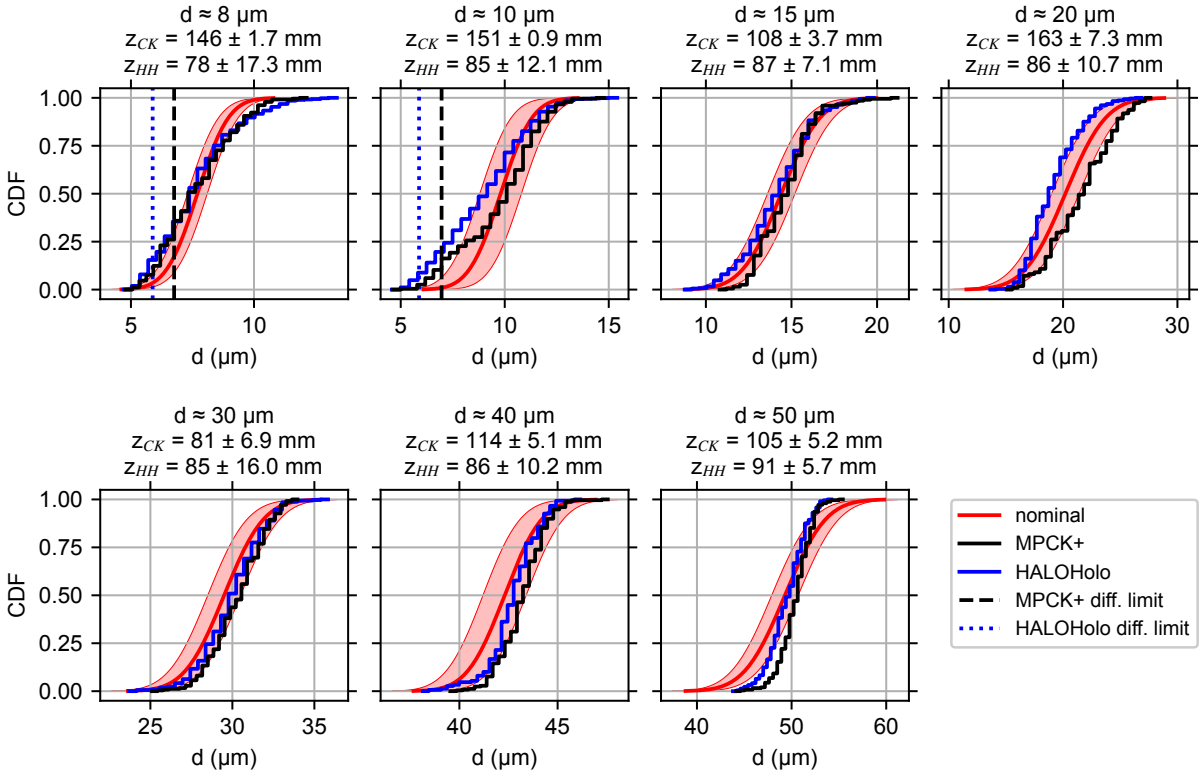


**Figure 4.** Comparisons of the CDFs of the particle diameters of Thermo Scientific Duke Standard 9000 Series glass microspheres from holograms taken by the MPCK$^+$ prototype holography system (black line), HALOHolo (blue line), and normal distributions with means and standard deviations from the manufacturer's calibration certificates for the particle batches (red line with pink for the 95% confidence interval for the mean); with a separate plot for each nominal particle size. The nominal particle size and the mean and standard deviation of the distance from the hologram plane ($z_{CK}$ for MPCK$^+$ and $z_{HH}$ for HALOHolo) is listed above each plot. For the two smallest sizes (top left), the distributions cross the diffraction limits ($d_{h,min,diff}(z)$ from Eq. S3 in the supplement) which are drawn as a vertical dashed black (MPCK) and dotted blue (HALOHolo) lines for comparison. The HALOHolo data is from Bagheri et al. (2021).

https://doi.org/10.5194/egusphere-2026-3456
Preprint. Discussion started: 1 July 2026


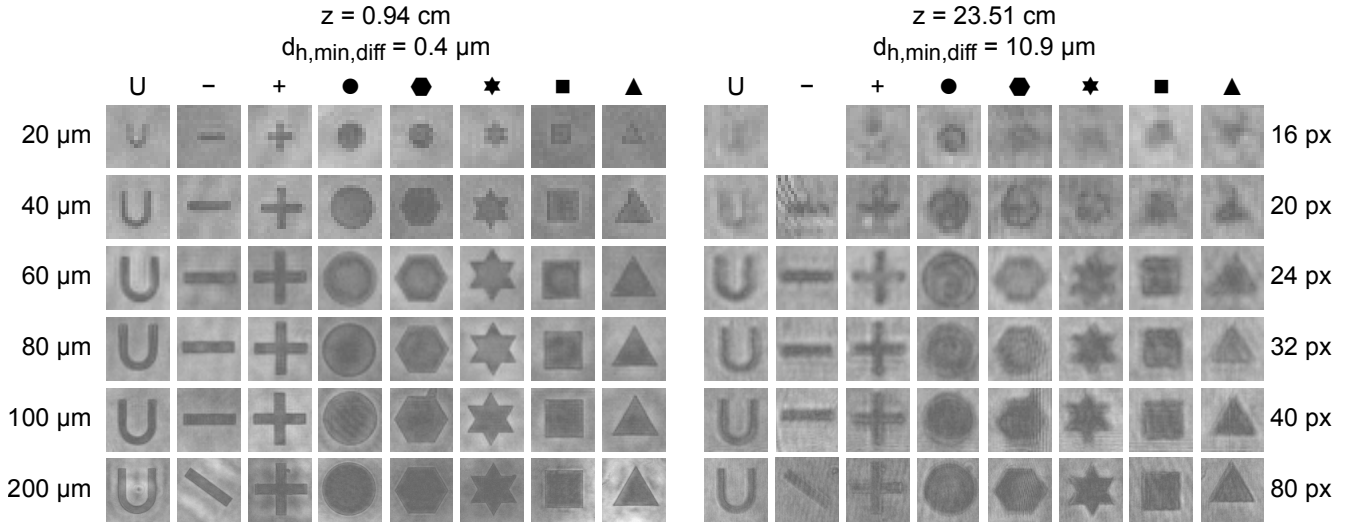


**Figure 5.** Cropped images of the grid of targets in the reconstructed slices from two holograms taken of the shape determination calibration mask, one taken near the camera (left) and one far from it (right). The distance from the hologram plane $z$ and the diffraction limit $d_{h,min,diff}$ (Eq. S3) for each hologram are listed at the top. The different target shapes are arranged horizontally with labels above the top row, and the different sizes are arranged vertically with the diameter of the circumscribed circles of the shapes for each size labeled on the left and the width of the cropped images in pixels (square crops) labeled on the right. Note that one pixel corresponds to 3 µm, the 20 µm minus sign could not be found at all for the far hologram, and the 200 µm minus sign is rotated on the slide (it detached, rotated, and re-attached).

cloud conditions (Schröder et al., 2024). Cloud droplets are typically small enough to serve as good natural flow tracers. For example, during EUREC$^4$A, the vast majority of drops had Stokes numbers (defined as the drop response time divided by the Kolmogorov timescale) below 0.01 (Schröder, 2023), while even for particles with Stokes numbers up to 0.1, flow-tracing errors are expected to be <1% (Tropea et al., 2007).

The optical and mechanical layout of the system is shown in Figure. 6. A dual-head Nd:YAG laser (Montfort PRI146 M-NANO PIV, 40 mJ per pulse, 4.2–4.4 ns, up to 15 Hz) generates the laser sheets. The beam is routed over a ∼2.5 m path on the MPCK$^+$ back plate via turning mirrors and expanded by a $-50$ mm cylindrical lens to form a thin sheet approximately 4 mm thick and 11 cm wide before reaching the PIV sampling volume, inclined by 30° from vertical (see also Figure 2). A custom in-house V-shaped beam block intercepts the laser sheet downstream of the measurement volume, providing approximately $\times 4000$ attenuation through multiple reflections. The camera is a Vision Research Miro R341 (2560×1600 px, 10 µm pixels), operated at 1280×920 px to enable PIV with short exposures. A Nikon 28 mm f/2.8 lens sets the required magnification and depth of field; a 535 nm (10 nm FWHM, OD 4) bandpass filter and a 75 mm AR-coated window suppress background light and protect the sensor. The resulting field of view is approximately 13.6 cm × 9.7 cm.

The PIV system captures image pairs at up to 15 Hz (30 frames per second, fps), while the holography camera operates at 75 Hz such that every fifth hologram is synchronised with a PIV pair. A microcontroller, triggered by the PIV camera operating

https://doi.org/10.5194/egusphere-2026-3456
Preprint. Discussion started: 1 July 2026


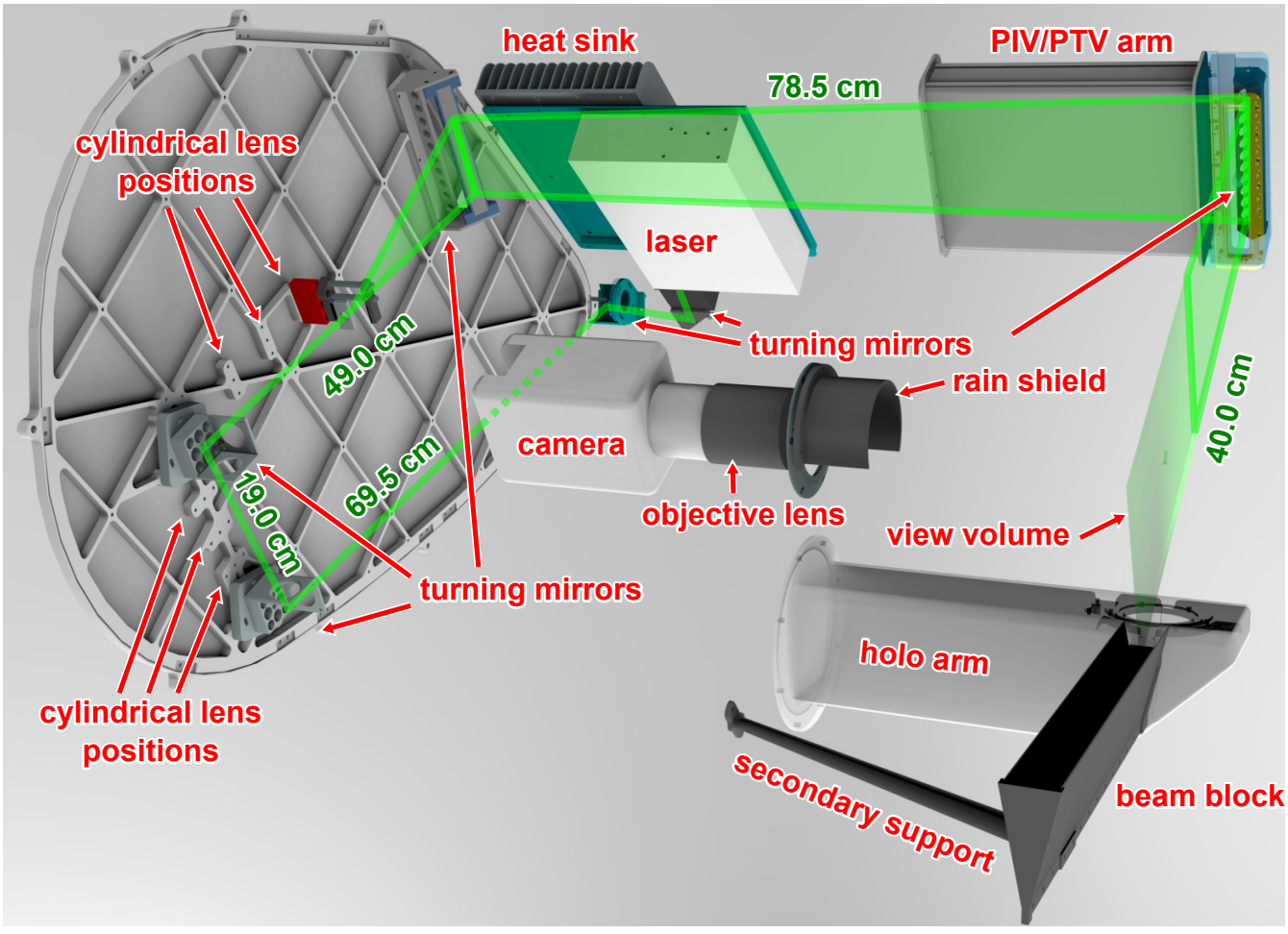


**Figure 6.** (a) Diagram of the 2-frame PIV system with labelled components and optics. The laser path (light green) shows the leg lengths in dark green; the final segment in the PIV arm is drawn to the center of the view volume.

at 2550 fps with a 380 µs exposure per frame, generates synchronisation signals for the PIV and holography lasers and cameras (see Figure S6 in the supplement). Following the first PIV laser pulse, and coinciding with every fifth holographic laser pulse, a second PIV pulse is emitted after a dynamically controlled delay $\Delta t_{piv}$ (typically 50–150 µs during EUREC$^4$A field campaign), determined from the true air speed measured by the 1D pitot tube. Although the PIV camera operates at 2550 fps, only frames corresponding to laser pulses are recorded, resulting in a net acquisition rate of 30 fps. As PIV images cannot be transferred to the computer in real time, they are first stored in the camera memory until it is full (approximately 120 s), after which they are transferred to the computer, a process that takes about 90 s. This cycle is repeated during in-cloud events until the available storage is filled, corresponding to a total acquisition time of approximately several hours.

https://doi.org/10.5194/egusphere-2026-3456
Preprint. Discussion started: 1 July 2026


The pulse separation $\Delta t_{piv}$ is adjusted automatically in flight to balance measurable displacement against in- and cross-plane particle loss from the light sheet. During EUREC$^4$A, most runs used 75–150 µs, depending on airspeed and turbulence intensity, yielding a velocity accuracy of $\sim 0.1$ m/s with sub-pixel displacement precision of $\sim 0.1$ pixel. Timing was verified using a photodiode, with inter-pulse delay errors below 1 µs, well within operational limits. This level of accuracy supports robust velocity gradient estimation for dissipation-rate retrieval in the volume co-located with the holography system.

Detection limits for the PIV system depend on droplet size, scattering angle, and ambient illumination. Mie scattering is strongest in the forward direction but remains significant at near-90° angles. We have carried out detailed simulations based on Mie theory, incorporating the imaging performance of the MPCK$^+$ PIV camera, objective optics, laser pulse energy, and beam expansion, indicate that for water droplets at near-90° scattering, minimum detectable diameters of $\sim 4$ µm during daytime and down to $\sim 2$ µm at night are achievable. Natural variability in cloud droplet number concentration (50–1000 cm$^{-3}$) is accounted for in the system design (e.g. sheet thickness and imaging magnification) to ensure sufficient seeding for correlation, without relying on laboratory-style optimisations such as extreme sheet narrowing or deliberate defocus, which are not practical under airborne conditions. In later sections, the in-situ performance of the PIV system is assessed in detail, including evaluation against the design goals and underlying assumptions.

## 5 Other Instruments

**Cloud Droplet Probe (CDP).** A SPEC Inc. FCDP (785 nm CW) provides particle-by-particle sizing for water droplets (2–50 µm reliably; larger detected but not sized) in a swept volume with 0.325 mm$^2$ frontal cross section. It is mounted on the front plate, ∼0.41 m aft and 0.08 m starboard of the particle imaging volumes (see Figure 2). The FCDP stores full Particle-by-Particle (PbP) data and 1 s summaries locally on a SD card, while reduced summaries are streamed via Ethernet to the MPCK$^+$ computer. It operates independently of other instruments, enabling autonomous triggering of imaging, redundancy, and cross-checks with PIV and pitot-derived airspeed.

**1D Pitot (airspeed, static pressure, temperature).** A Simtec/Swiss-Airdata HPS-1 (200 mm) with PSS8 scanner and Pt-100 RTD supplies real-time airspeed and pressure/temperature. It is optimized for low-speed operation and tolerates half-cone incidence up to ∼25° with $< 5\%$ airspeed error, a criterion met in all flights. During EUREC$^4$A, boxcar averaging set the effective sampling near 12.5 Hz; the PSS8 airspeed statistics over the last minute (minimum, maximum, standard deviation) were used to adapt the PIV pulse separation $\Delta t_{piv}$ on each run. The PSS8 barometric altitude provides a safety fallback for laser shutdown logic.

**3D Pitot (five-hole probe).** A Vectoflow five-hole pitot tube with an SVMtec PSC-5 scanner measures 3D velocity vectors (up to 100 Hz). The probe accepts angles of attack up to ∼50° and was mounted on the Eulerian module upwind of the MPCK$^+$ instrument(Fig. 2). Early MSM82/2 flights had the reference port inside the hull; subsequent flights vented outdoors and earlier data were corrected offline using 1D pitot pressure.

**Humidity (RHT).** One or two capacitive RH/temperature sensors (Aosong AM2315; previously UPSI F-TUTN.43 fast RHT) are mounted in a 3D-printed radiation shield on the upper port side (marked as RH/T in Figure 2). The UPSI sensor

https://doi.org/10.5194/egusphere-2026-3456
Preprint. Discussion started: 1 July 2026


proved to be unreliable during field tests and was therefore not used beyond the first two campaigns. The more robust Aosong AM2315 sensor, however, provides continuous measurements of air thermodynamic properties and enables cloud detection and confirmation. RHT data are read by a dedicated microcontroller and forwarded to the MPCK$^+$ computer. The current MPCK$^+$ humidity sensors (two Aosong AM2315 sensors) have a relatively long response time of approximately 30–60 s and therefore resolve only large-scale variability.

It should also be noted that an LDV (MSE miniLDV-G5 custom, 658 nm) was trialled for aft-directed velocity but proved operationally fragile (communications/download issues) and was removed after MSM82/2 to save mass and power. The Particle Imaging system (inline holography and two-frame PIV), described above, already provides the collocated size–position–velocity reference for cross-validation with the swept-volume instruments.

## 6 Supporting Systems: Navigation, Video, and Other Infrastructure

**Navigation (INS/GNSS).** The MPCK$^+$ instrument uses an SBG Ellipse series INS (Ellipse-N during MSM82/2; Ellipse2-D thereafter) combining IMU and GNSS for position, velocity, roll/pitch/yaw, and angular rates. A backup GNSS (Garmin 15xH during MSM82/2; u-blox NEO-M8U thereafter) connects directly to the Power Board for resilience and logging when the main computer is off. These data enable geolocation, altitude-based interlocks, motion diagnostics, and frame transforms.

**Diagnostic Video.** Two low-power serial JPEG cameras (Putal PTC06 inside; PTC08 in a waterproof housing outside) provide situational awareness and post-flight diagnostics at ∼1 frame per 15–20 s. The flight camera views the CDP, holography arms, PIV sheet/beam block, and forward scene, allowing confirmation of cloud entry, hardware integrity, and qualitative flow alignment.

**Brief summary of remaining subsystems.**

- *Radio communication links:* Two primary long-range links (Digi XBee Pro S2C at 2.4 GHz; Digi SX868 at 868 MHz) plus a backup LoRa (RFM96W at 433 MHz) provide command/telemetry redundancy. The platform is fully autonomous to tolerate no or intermittent radio links. All the data are stored locally and only monitoring information are sent via radio links.
- *Power/Control:* A custom Power Board manages DC rails, battery with dedicated battery management system, safety relays, and laser interlocks; instruments can be powered/cycled individually.
- *Laser Safety:* A certified Class 1-equivalent operational envelope at 15 m is achieved via enclosure/beam blocks, safety relays, E-stop/key-switch, altitude-based interlocks (e.g. laser operation only 400 m above ground level), and a strong strobe indicator.

https://doi.org/10.5194/egusphere-2026-3456
Preprint. Discussion started: 1 July 2026


## 7 In-situ Performance Evaluation

In the following subsections, we assess the performance, validity, and reliability of the MPCK platform and the MPCK$^+$ instrument using data from earlier field campaigns (mainly EUREC$^4$A). Owing to the novelty of the system and the built-in measurement redundancies, we compare subsystems against each other as well as additional measurements carried out in the lab against other references to quantify accuracy and robustness, highlight the strengths and limitations of each measurement, and specify the conditions under which the resulting scientific conclusions are reliable.

### 7.1 Temperature and Humidity Measurements: Lab calibrations and in-situ intercomparison with radiosondes

The RHT sensors of the Humidity system and the temperature sensor of the 1D pitot tube were calibrated in the lab. For the humidity calibration, an airtight chamber kept at room temperature and having a fan for circulating and mixing the air inside was used to produce reference relative humidities. The sensor to be calibrated and two NTC probes were placed in the calibration chamber. The NTC temperature sensors had been calibrated to within ±30 mK against a NIST-traceable Lakeshore Pt103. One NTC probe measured the air temperature in the vicinity of the RHT sensor being calibrated and the the other measured the temperature of a supersaturated brine which was in an open petri dish. From the temperatures of the air and the brine and the specific salt that is used to make the brine, the actual relative humidity can be calculated. We used a non-toxic and non-corrosive subset of the brines and their published saturated humidities from Greenspan (1977). The salts used in our calibration were lithium chloride (LiCl), potassium acetate ($CH_3COOK$), magnesium chloride ($MgCl_2$), potassium carbonate ($K_2CO_3$), sodium bromide (NaBr), sodium chloride (NaCl), potassium bromide (KBr), potassium chloride (KCl), and potassium sulfate ($K_2SO_4$). In addition, one run to measure at saturation was done with distilled water and another run to measure at zero relative humidity was done by putting dry water-free calcium chloride ($CaCl_2$) into the petri dish. For the saturated vapor pressure in air as a function of temperature at the sensor being calibrated, we used the fit from Murphy and Koop (2005). Using Murphy and Koop (2005) is admittedly overkill given the measurement uncertainties of our sensors when Eq. 4.B.1 from WMO (2018) would have sufficed, but it was used for consistency with possible future calibrations if we eventually fly the CloudKite in clouds with supercooled water and/or ice and because we intend to use it for our data processing tool-chain. Quadratic polynomial fits were used.

Temperature calibration was done by intercomparison with the NTC sensor measuring the air temperature of the air in the vicinity of the sensor. This was done both using the data taken during the calibration of humidity and additional lower and higher ambient air temperatures in the 10–30 °C range, which was the expected temperature ranges to be measured during MSM82/2 and EUREC$^4$A. Linear calibration polynomials were used. As the slopes from linear fits were extremely close to one over the temperature range, we set the slopes to one and the offsets to the mean deviations (essentially, offset only fits).

We have also compared our relative humidity and temperature measurements to those obtained by nearby radiosondes during EUREC$^4$A. In total, 10 events with radiosoundings during the flight of the MPCK$^+$ could be identified from 5 flights. Here, we compare the measurement of temperature, relative humidity and dewpoint between the MPCK$^+$ instrument and the radiosonde and discuss effects of thermal mass and other potential influences on the measurements.

https://doi.org/10.5194/egusphere-2026-3456
Preprint. Discussion started: 1 July 2026


**Table 2.** Comparison of measured temperature ($T$), relative humidity (RH), and dew point temperature ($T_d$) between the radiosonde and both AM2315 sensors of the MPCK$^+$. Radiosonde values serve as the reference, with deviations ($\Delta$) of AM2315-1 and AM2315-2 reported at altitude levels closest to the MPCK$^+$ at the same time. Summary statistics include mean deviation, median, and standard deviation (std). Date and time in bold indicate daytime measurements, while all others were taken at night.

| Flight | Date | Alt. | Radiosonde | | | AM2315-1 ($\Delta$) | | | AM2315-2 ($\Delta$) | | |
|---|---|---|---|---|---|---|---|---|---|---|---|
| | | $z$ [m] | $T$ [K] | RH [%] | $T_d$ [K] | $T$ [K] | RH [%] | $T_d$ [K] | $T$ [K] | RH [%] | $T_d$ [K] |
| 6 | **2020-02-04** | 1030 | 292.4 | 80.4 | 289.0 | -0.2 | +3.1 | +0.4 | +0.1 | +1.4 | +0.3 |
| 11 | 2020-02-11 | 1060 | 291.0 | 76.2 | 286.7 | +0.1 | +5.1 | +1.1 | +0.7 | +1.7 | +1.1 |
| 12 | 2020-02-12 | 910 | 291.3 | 100.0 | 291.3 | +0.6 | -5.9 | -0.3 | +1.2 | -11.5 | -0.8 |
| 16 | 2020-02-15 | 190 | 298.0 | 77.5 | 293.9 | +0.5 | +0.3 | +0.4 | +0.7 | -0.8 | +0.4 |
| 16 | 2020-02-16 | 730 | 293.3 | 99.5 | 293.2 | -0.2 | -5.2 | -1.0 | -0.1 | -5.3 | -1.0 |
| 16 | 2020-02-16 | 980 | 291.1 | 96.2 | 290.5 | -0.1 | +2.8 | +0.4 | +0.1 | +3.5 | +0.7 |
| 20 | 2020-02-17 | 880 | 292.3 | 75.7 | 288.0 | +0.2 | -1.6 | -0.2 | +0.7 | -3.1 | -0.1 |
| 20 | 2020-02-18 | 920 | 292.5 | 80.8 | 289.1 | 0.0 | +1.5 | +0.3 | +0.2 | -0.2 | +0.2 |
| 20 | 2020-02-18 | 890 | 292.3 | 88.2 | 290.4 | -0.3 | +5.0 | +0.5 | -0.2 | +4.4 | +0.5 |
| 20 | **2020-02-18** | 960 | 292.1 | 87.3 | 289.9 | -0.8 | +9.5 | +0.9 | -0.5 | +6.4 | +0.7 |
| **Summary** | | | Mean | Mean | Mean | +0.02 | +0.36 | +0.31 | +0.3 | -0.35 | +0.21 |
| | | | Med. | Med. | Med. | +0.1 | +1.5 | +0.3 | +0.2 | +1.4 | +0.3 |
| | | | Std | Std | Std | 0.4 | 4.0 | 0.5 | 0.5 | 4.5 | 0.5 |

For temperature ($T$), sensor AM2315-1 exhibits a small average bias of +0.02 K with minimal deviation from the radiosonde reference. AM2315-2 shows a slightly higher bias of +0.3 K, indicating a tendency to read marginally warmer than the radiosonde. For relative humidity (RH), AM2315-1 slightly overestimates the radiosonde values with a bias of +0.36%, whereas AM2315-2 shows a negative bias of -0.35%, indicating a slight underestimation of RH in most cases. The response time of both temperature and humidity sensors ranges between 15–30 s and varies considerably with wind speed. Within clouds, MPCK$^+$ measurements of RH often exceeds 95% but rarely reaches the expected 100% (as observed by radiosondes). This discrepancy likely arises from the sensor and protective cap design, as well as the thermal mass of MPCK$^+$ instrument. Under cloudy or high-humidity conditions, sensor drying can be slow, delaying recovery to free-atmosphere values — an effect that is difficult to quantify a priori. These limitations should therefore be considered when interpreting the measurements. For dew point temperature ($T_d$), both AM2315-1 and AM2315-2 show small positive biases but remain within 0.5 K of the radiosonde on average. On average, AM2315-1 provides the most consistent agreement with the radiosonde. AM2315-2 exhibits slightly higher $T$ and lower RH, indicative of minor calibration differences. Both sensors remain within acceptable accuracy limits for profiling, particularly under cloud-free conditions, while in-cloud measurements of temperature and relative humidity should be used with caution.

https://doi.org/10.5194/egusphere-2026-3456
Preprint. Discussion started: 1 July 2026


### 7.2 The influence of MPCK$^+$instrument mounting method on velocity measurements

One of the key criteria for evaluating measurements, particularly air velocity and turbulence characteristics, on a passively controlled platform such as the MPCK platform is the flight stability and the potential influence of platform geometry, mounting strategies, and platform motion on the measurements. It has been shown that platform-induced disturbances, such as oscillations, are typically isolated within certain frequency ranges which can be easily mitigated, e.g. by using unaffected regions of the turbulence inertial sub-range for measuring the energy dissipation rate Schröder (2023). By comparison with simulations of turbulent flow fields carried out using direct numerical simulations, it has also been shown that having a freely rotating measurement platform that aligns with local flow directions at various spatio-temporal scales, instead of being fixed with respect to the global mean flow direction, has minimal impact on the turbulence characterization of the flow Schröder (2023).

To quantify the strength and frequency of the angular dynamics of the MPCK$^+$ instrument, here we assess flight stability, the roll and pitch angles of the MPCK$^+$ instrument for different mounting positions across two field campaigns and multiple mounting positions as summarised in Table 3. It should be noted that the mean yaw angle is determined largely by the true wind direction at the height of the instruments and is therefore less relevant to the stability discussion. Mean values of pitch and roll angles are controlled mainly by the initial mounting configuration (e.g. the relative length of attachment ropes used in spar-mount method) rather than by wind conditions and should not be considered as a measure of flight stability. However, large mean values of the pitch angle can cause strong aerodynamic interference and degrade instrument performance. For example, the 1D pitot tube maintains <5% error only for half-cone incidence angles below 25°, a criterion satisfied in all flights. Flight stability is best gauged by the temporal variability (e.g. standard deviation) of pitch and roll. As summarized in Table 3, the tether-mount shows the smallest deviations (<2.5°), the keel-mount is intermediate, and the spar-mount is least stable (up to 15.0°).

**Table 3.** Mean and standard deviation (in bold) of pitch and roll of the MPCK$^+$ instrument during various flights. Results are shown for EUREC$^4$A (Flights 3–20) and selected PaCE flights (Flights 21–26). Schematics of various mounting positions are shown in Figure 1.

| | keel-mount | spar-mount | | | | | | tether-mount | | |
|---|---|---|---|---|---|---|---|---|---|---|
| Angles [°] | Flight 3 | Flight 6 | Flight 9 | Flight 12 | Flight 16 | Flight 18 | Flight 20 | Flight 21 | Flight 25 | Flight 26 |
| Pitch | 9.4 ± **2.3** | 2.7 ± **15.0** | 16.8 ± **8.9** | 18.2 ± **7.0** | 23.2 ± **13.9** | 15.0 ± **13.5** | 17.1 ± **10.8** | -1.4 ± **1.6** | 4.6 ± **1.8** | 5.9 ± **1.4** |
| Roll | -24.0 ± **4.0** | -0.4 ± **3.7** | -2.0 ± **4.7** | 1.8 ± **3.7** | 4.7 ± **11.1** | -2.9 ± **14.5** | 0.9 ± **8.2** | 3.7 ± **1.8** | 3.0 ± **2.5** | 1.6 ± **0.5** |

Analysing the frequency spectra of the Euler angles clarifies how mounting affects the MPCK$^+$'s dynamics. Here, we first focus on the EUREC$^4$A campaign and examine two-minute intervals from two flights carried out on two different days (Flights 3 and 6), during which concurrent 1D and 3D pitot measurements were collected. As shown in Figure 7, both pitch and roll exhibit dominant peaks between roughly 0.1 and 1.0 Hz, while the keel-mount shows a negligible peak compared with the spar-mount. Comparable behaviour is also observed for the tether-mount, even though the pitch/roll standard deviations are the smallest for this mounting method. As detailed in section 1.2 of the supplementary information, tether-mounted MPCK$^+$ still

https://doi.org/10.5194/egusphere-2026-3456
Preprint. Discussion started: 1 July 2026


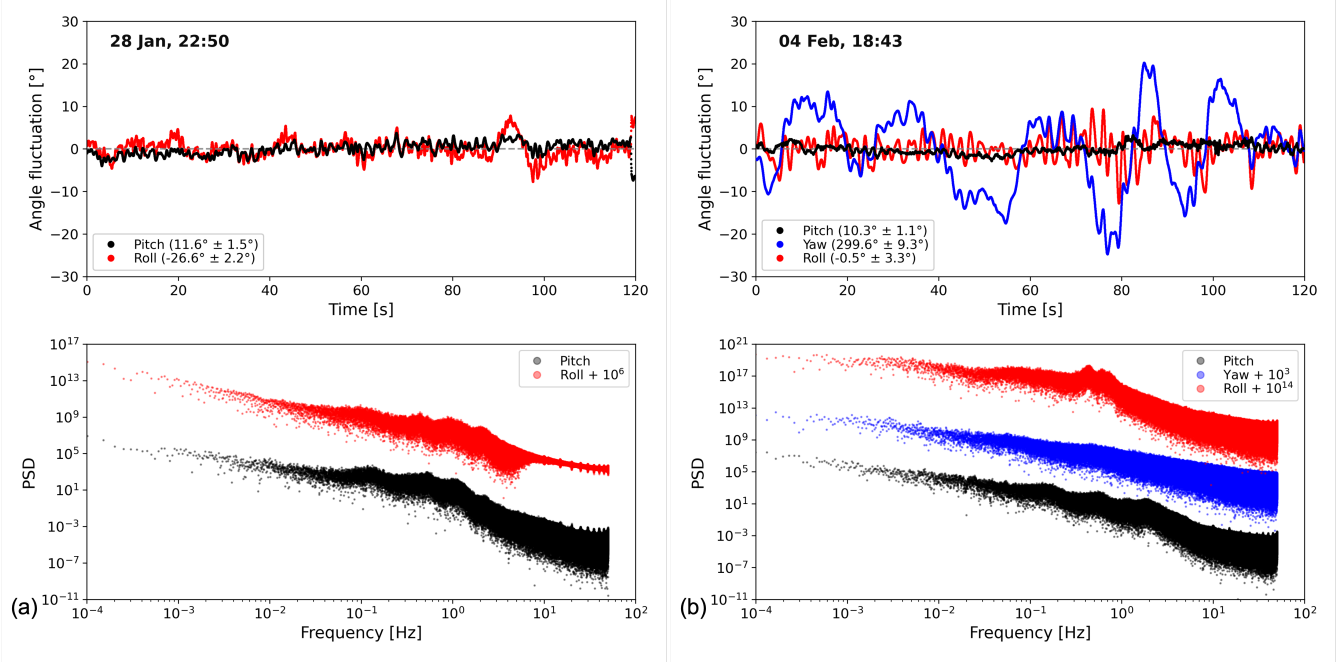


**Figure 7.** The MPCK$^+$'s pitch, roll and yaw angles and their corresponding power spectral densities for (a) Flight 3 (January 28, 22:50) using the keel-mount configuration and (b) Flight 6 (February 4, 18:43) using the spar-mount configuration. Values in parentheses indicate the mean and standard deviation, respectively. All Euler angle curves are vertically shifted to have zero mean. The yaw angle is omitted in (a) because the INS could not reliably determine the heading.

exhibits dominant peaks near 0.05 and 0.5 Hz, indicating that these motions primarily reflect the inherent dynamics of a tethered aerostat. Mitigating the impact of these oscillations on turbulence estimates is an important concern. Although INS-based motion corrections are, in principle, feasible, the EUREC$^4$A INS data were too noisy or insufficiently sampled for the high-frequency data ($\sim$ 100 Hz), and yaw was degraded by electromagnetic interference. Importantly, the oscillations are spectrally localized (Fig. 7), which allows us to extract turbulence statistics outside the dominant motion bands and to limit contamination of the scales of interest as discussed above and also will be shown in the next section.

### 7.3 Aerodynamic Influences of the MPCK$^+$ Body and Associated Corrections

As is the case for any measurement probe, an important calibration step is to understand the aerodynamic disturbances caused by the probe body. For wind-speed sensors such as pitot tubes and the PIV, corrections are required to accurately assess turbulence, while for the FCDP, corrections are needed to compute the true swept probing volume for droplet concentration measurement. By placing the MPCK$^+$ instrument in a wind tunnel, we investigated the presence of aerodynamic disturbances and the feasibility of deriving reliable, consistently applicable corrections from calibration measurements. To quantify these body effects, the MPCK$^+$ instrument is placed inside a wind tunnel at various far-field wind speeds ranging between 5.3 m/s and 9.8 m/s, and the local wind speed is measured at several positions around and within its sampling volume: far from the setup, at

https://doi.org/10.5194/egusphere-2026-3456
Preprint. Discussion started: 1 July 2026


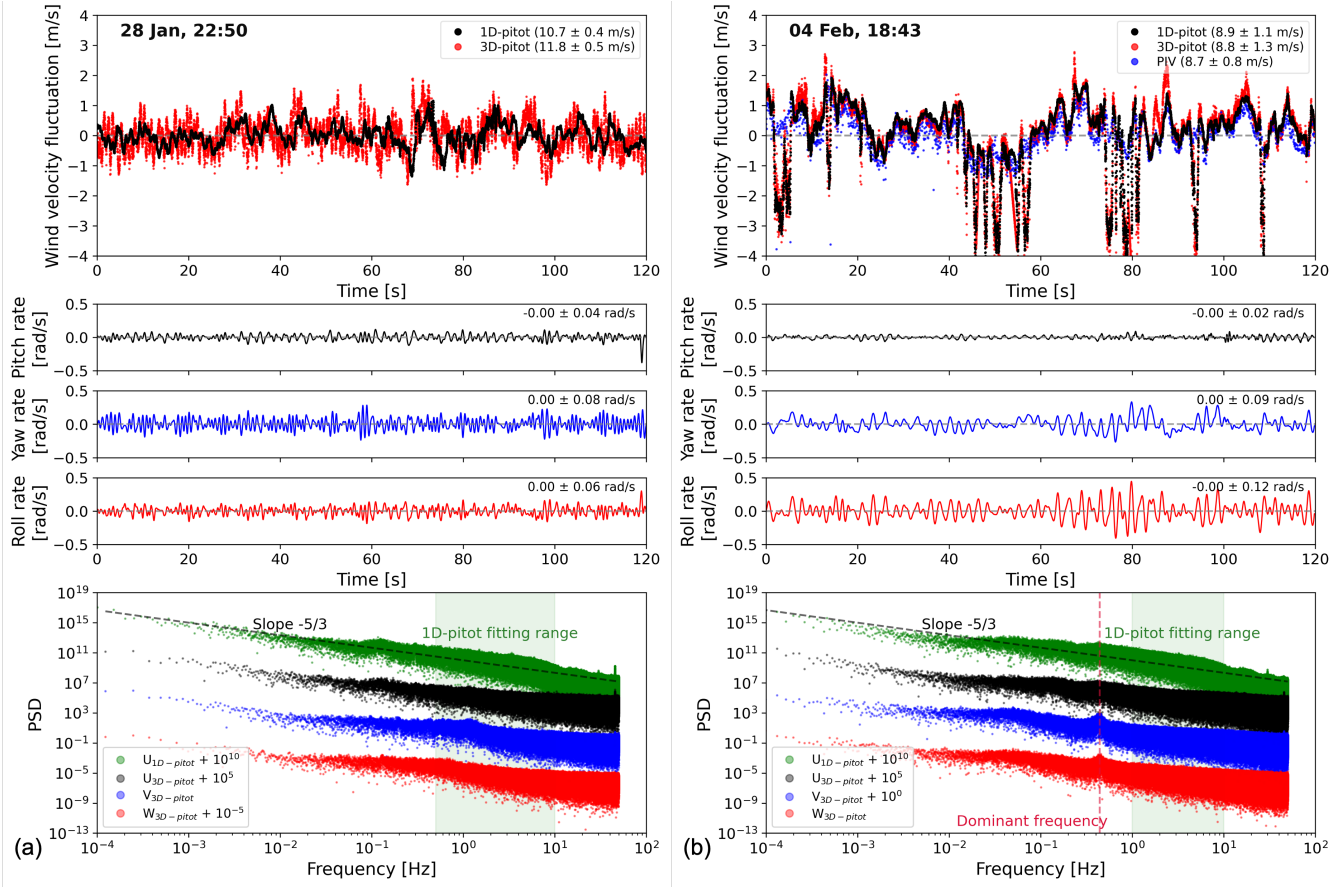


**Figure 8.** Measured wind-velocity components, MPCK$^+$ angular rates, and the power spectral density (PSD) of wind-velocity components for two example flights: (a) January 28, 22:50 (subset of Flight 3, keel-mount, 1D and 3D pitot data available) and (b) February 4, 18:43 (subset of Flight 6, spar-mount, 1D, 3D pitot and PIV data available). The top subpanels show mean-subtracted wind velocity from the pitot tubes, the middle subpanels show angular rates (rates of pitch, yaw, and roll), and the bottom subpanels show the corresponding PSDs of the wind-velocity components. Wind-velocity time series are de-trended to remove effects of altitude changes during these time windows. The dashed line marks the dominant pendulum frequency of the MPCK$^+$; the green band denotes the frequency range used to fit the second-order structure function for the 1D pitot tube. The $U$, $V$, and $W$ components are defined with respect to the MPCK$^+$ geometry as shown in Figure 2.

https://doi.org/10.5194/egusphere-2026-3456
Preprint. Discussion started: 1 July 2026


the tips of the pitot tubes, at various locations in the PIV sheet, between the FCDP arms, and at other locations. On average, the MPCK$^+$ 1D pitot measured $0.647 \pm 0.05$ times the far-field wind speed and the PIV centre $1.3 \pm 0.03$ times, yielding a PIV-to-1D-pitot ratio of $2.00 \pm 0.11$, consistent with measured field data. The 3D pitot tip and FCDP midpoint measured $0.547 \pm 0.027$ and $1.09 \pm 0.04$ of the free-stream wind, respectively. No correlation between the correction values and the far-field wind speed is found, which enables a straightforward application of these corrections to the field measurements.

Figure 8 shows the corrected velocities for two flights, with close agreement between 1D and 3D pitot measurements. Velocity fluctuations are larger in Flight 6 (spar-mount) than in Flight 3 (keel-mount), despite higher mean wind speed in Flight 3, likely due to platform-induced motion. This interpretation is supported by the PIV measurements, which are effectively instantaneous (approximately 100 µs pulse separation between two frames) and therefore insensitive to the dominant platform oscillations at 0.1–1.0 Hz, see Figure 7 (detailed information on PIV postprocessing methods and turbuelnce characterization are provided in the folloiwng sections). The turbulence energy dissipation rate, for example, can still be calculated by excluding the primary platform-induced oscillation range, as indicated in the lower panels of Figures 8a and b.

The middle panels of Figures 8a and b show the angular rates of the MPCK$^+$ instrument during the velocity measurements. As discussed previously, the keel-mounted configuration exhibits lower angular rate fluctuations than the spar-mounted configuration. In particular, the RMS roll angular rate is approximately half in the keel-mount case, reflecting the dominant pendulum motion of the platform. Except for the yaw rate and the 3D pitot tube, the angular rates show weak correlation with the velocity measurements (see Figure 9b).

Given that the PIV measurement plane is offset from the platform's centre of mass by up to 0.5 m and the maximum angular rate is about 0.4 rad s$^{-1}$, the resulting induced linear velocity error is estimated to be below 0.2 m s$^{-1}$, corresponding to less than 2% of the mean wind speed. Furthermore, this angular motion could affect the estimated velocity gradient (turbulent energy dissipation rate; see Section 7.4) nonlinearly across the measurement plane. This error is typically very low in the majority of situations, remaining below 1%. Even when the maximum observed angular velocity ($\sim 0.3\,\mathrm{rad\,s^{-1}}$) is taken into account, the induced velocity gradient error remains below 0.1% at the PIV-plane centre and increases to approximately 1% near the edge of the image. In the central region selected for the calculation of the energy dissipation rate (see Section 7.4), the error in dissipation rate due to the nonlinearity is estimated to be less than 0.05%.

To evaluate the robustness of the velocity measurements against platform motion, Figure 9 presents the correlation coefficients between the Euler angles and their time derivatives (angular rates) with the velocity components measured by both the pitot tubes and the PIV system. In Figure 9a, pitch (which sets the flow incidence on the system) correlates at 0.1–0.4 with all sensors. By contrast, PIV shows much lower correlations with yaw and roll (<0.1) than the 1D and 3D pitot tubes (0.3–0.6), indicating that it is associated with a low sensitivity to platform motions. Angular rates are weakly correlated with all sensors, except for yaw with the 3D pitot tubes, implying that rotational motion is largely small relative to sensor signal-to-noise and only weakly imprinted on the measurements. Overall, the PIV measurements are demonstrated to be robust against platform-induced motions.

https://doi.org/10.5194/egusphere-2026-3456
Preprint. Discussion started: 1 July 2026


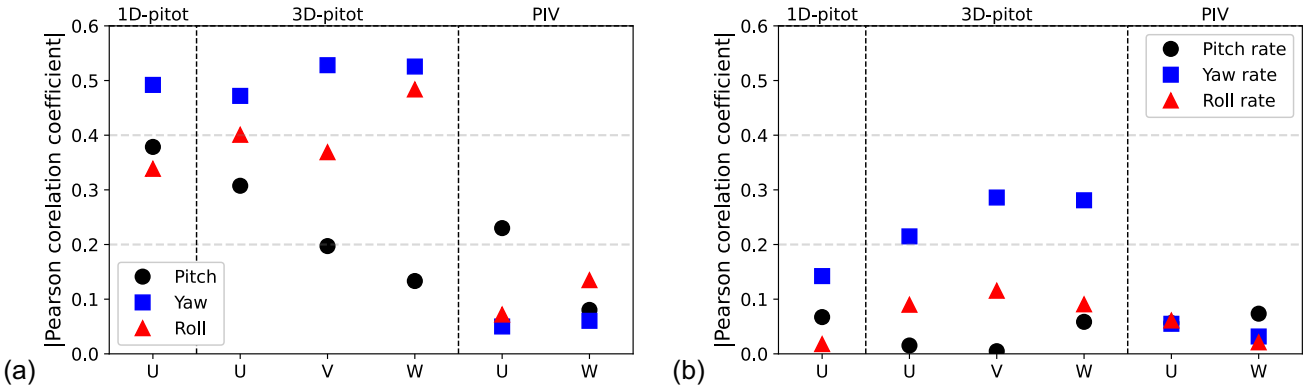


**Figure 9.** Magnitude of the Pearson correlation coefficients between wind-velocity components measured by the pitot tubes and the PIV for spar-mounted MPCK$^+$ instrument (a) Euler angles, (b) angular velocities, for multiple measurement methods during a subset of Flight 6 (February 4, 18:43).

## 7.4 PIV Post-Processing

Here, we use airborne measurements inside shallow cumulus clouds to assess the performance of the PIV system under variable and unpredictable field conditions. The methods applied to extract velocity and turbulence features are also presented and evaluated. A key advantage of the PIV measurements over conventional anemometers is its ability to measure two-dimensional velocity fields within a single localised snapshot inside clouds, producing a large number of velocity vectors from which local turbulence features can be reliably estimated when properly processed. In addition, it can reveal aerodynamic disturbances (e.g. from the holography arms or unfavourable wind directions) at the time of measurement, providing in-situ diagnostics for data quality and validation. This is an extremely important and unique capability of the MPCK$^+$.

Here, MPCK$^+$ PIV data are analysed using LaVision DaVis 8 softer after image pre-processing and background removal. The background is estimated as the minimum intensity of each image pair, followed by a median filter (3-pixel kernel), and then subtracted from each raw image. Displacement vectors are computed using adaptive multi-pass cross-correlation, with interrogation window sizes reduced from 128 to 64 pixels and a 50% overlap. To mitigate peak locking, given near single-pixel particle images, symmetric sixth-order spline interpolation is applied, achieving a nominal displacement uncertainty below 0.05 pixels (Michaelis et al., 2016).

Figure 10 illustrates various aspects of sample PIV data from a day flight during EUREC$^4$A field campaign (February 4th, 2020). Panel (a) shows a projection of 3600 background-removed PIV images, where the maximum pixel intensity across all images is displayed. Cloud droplets appear as bright pixels against a dark background, with the mean wind direction being from the top right corner to the bottom left corner when the MPCK$^+$ pitch angle is 0°. The holographic volume is outlined with yellow dashed lines, with the upper and lower arms extending about 5 cm beyond the shown window (see also Figure 2). The

https://doi.org/10.5194/egusphere-2026-3456
Preprint. Discussion started: 1 July 2026


left side of the image is brighter than the right, indicating higher droplet detection efficiency, primarily due to the transition from forward to backward scattering, and partly because the laser beam diverges from left to right as discussed in section 4.2.

For the PIV analysis, the PIV images are divided into interrogation windows. For each window, a velocity vector is determined. Only interrogation windows with a cross-correlation peak ratio >1.3 and at least 20 particles are considered valid, following conservative PIV analysis guidelines to ensure high sub-pixel accuracy in displacement estimation (Tropea et al., 2007). This also excludes regions where insufficient droplet seeding, due to natural cloud inhomogeneities, prevents reliable tracking within the final 64 pixel window. Furthermore, interrogation windows with velocity vectors deviating by more than 1% from the main wind direction (defined as the median velocity direction in the centre of the PIV image) are flagged as invalid (see Figure 10d) to exclude regions potentially affected by the holographic arms. The 1% threshold was determined by evaluating multiple threshold values below 5% and selecting a conservative limit for which dissipation-rate estimates remain unchanged. After removing invalid windows, the average seeding density across all subsets is about 0.01 ppp (range 0.006–0.015 ppp). The final valid window fraction after applying all criteria to the 1800 vector fields (from an example 3600 images in a 2 min PIV run) is shown in Figure 10b, with colour indicating the fraction of valid vectors. Most valid vectors are concentrated along diagonal regions of the PIV images and align with the expected mean flow direction.

Figure 10c shows the velocity magnitude from a single PIV image pair, highlighting both the highly resolved velocity field within clouds and also flow inhomogeneities induced by the previous (less-aerodynamic) version of holographic arms during EUREC$^4$A. The flow accelerates from the top-right to the lower-left corner, where it is constricted between the arms, and a pronounced disturbance is visible near the upper arm, which lies closest and directly upstream of this region. In contrast, the lower arm has a weaker influence, as its nearest location in the PIV image lies upstream of the sampling region.

These measurements enable quantitative assessment and correction of instrument-induced flow disturbances. In addition to the median flow direction constraint (the 1% wind-direction deviation criterion) and other data-quality filters described above, systematic velocity biases are mitigated by removing linear trends in both the streamwise and cross-stream directions. This is achieved by combining all independent velocity fields within each two-minutes PIV run and applying linear regression-based de-trending along rows and columns of interrogation windows. Velocity gradients are then computed using a second-order central difference scheme, while rows or columns with fewer than five valid windows are excluded. Within the final selected regions, in the example shown here, the velocity magnitude ranges from 8.59 to 8.85 m/s, with a standard deviation of 0.05 m/s, reduced from 8.67–9.88 m/s and 0.34 m/s prior to de-trending. This indicates an approximately uniform velocity field and confirms that the influence of the arms has been largely mitigated.

Several methods exist to estimate energy dissipation rates from PIV measurements, including two-dimensional spatial velocity gradient methods with local axisymmetry (George and Hussein, 1991) or isotropy assumptions (Tanaka and Eaton, 2007; Verwey and Birouk, 2022), one-dimensional energy spectra (Doron et al., 2001), and longitudinal second-order structure functions (Schröder et al., 2024). For spatial gradient methods, the interrogation window size should be close to the Kolmogorov scale. Using 0.1–0.5 times the Kolmogorov length scale, errors of only a few percent are achievable with corrections (Tanaka and Eaton, 2007), whereas window with 0.8 times the Kolmogorov length yields 10–20% errors (Verwey and Birouk, 2022). Minimizing uncertainty also requires sufficient seeding density, as measurement error decreases with more particles per pixel.

https://doi.org/10.5194/egusphere-2026-3456
Preprint. Discussion started: 1 July 2026


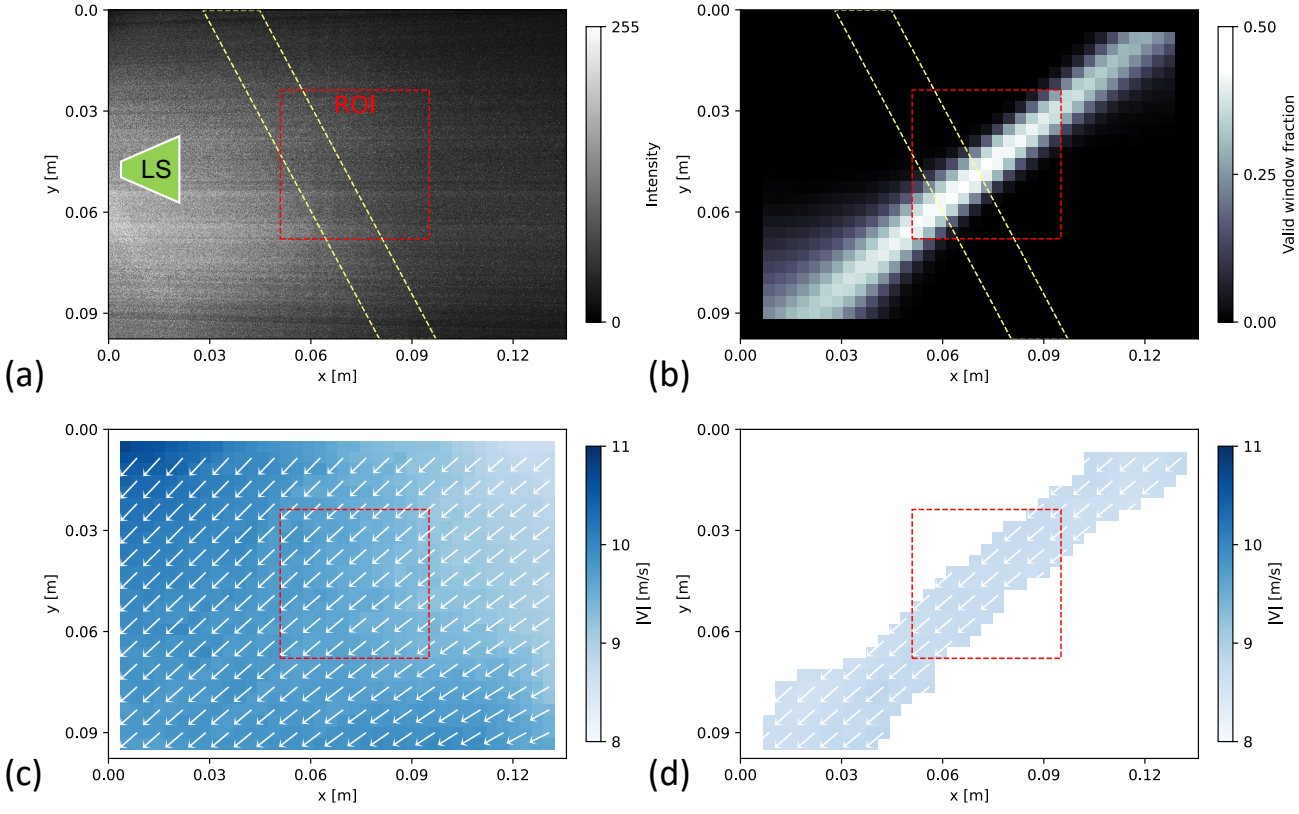


**Figure 10.** Example PIV measurements on 4 February, 18:43 (subset of Flight 6). (a) Maximum intensity image obtained by taking the pixel-wise maximum over a two-minute PIV run (3600 images). The central region of interest (ROI), used to estimate the energy dissipation rate and mean flow properties, is indicated by the red dotted square. The overlap with the holographic beam, aligned with the gravity vector, is shown by yellow dashed lines. The green laser sheet symbol (LS) indicates the beam propagation direction, which expands vertically and decreases in intensity from left to right due to divergence. (b) Fraction of valid PIV interrogation windows over 3600 images after applying quality filters, including a minimum of 20 particles per window and a maximum deviation of 1% from the mean wind direction. (c) Velocity magnitude field for a single PIV image pair over the full field of view. (d) Same as (c), after removal of systematic velocity biases induced by the holographic arms and masking of invalid regions, showing only windows within 1% of the mean wind direction and with $\geq$20 particles per window. For this dataset, the mean flow direction is 137.3° (standard deviation 0.7°), estimated from the median velocity angle within the central ROI. For clarity, every second velocity vector is shown in (c) and (d).

https://doi.org/10.5194/egusphere-2026-3456
Preprint. Discussion started: 1 July 2026


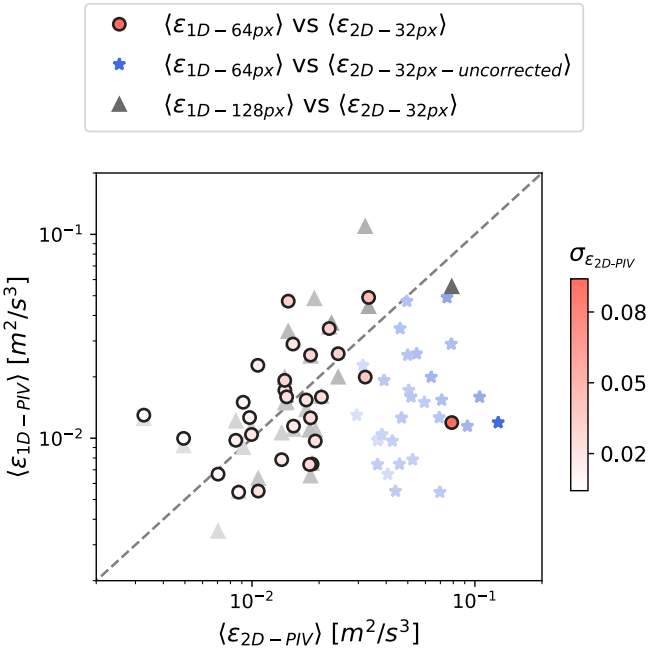


**Figure 11.** Comparison of energy dissipation rates estimated from 1D and 2D PIV. Each marker represents the mean dissipation rate for one of 30 PIV subsets collected during EUREC$^4$A. Each subset spans approximately two minutes; however, in-cloud data usually occupy only a fraction of this duration, typically 30–90 seconds per subset. Circles indicate 1D interrogation windows of 64 pixels and 2D vector spacing of 32 pixels, obtained from 64-pixel interrogation windows with 50% overlap. Stars show the same settings but without velocity bias correction. Triangles correspond to 1D windows of 128 pixels and 2D spacing of 32 pixels. The marker opacity represents the standard deviation of the 2D PIV dissipation rate during the measurement interval, as shown in the color bar. On average, the ratio of 2D (32-pixel spacing) to 1D (64-pixel window) dissipation rates is $1.3 \pm 0.8$. Here, both the 2D (32-pixel spacing) to 1D (64-pixel window) PIV have the same interrogation window size of 64 pixels.

Additionally, particle image diameters of 2–3 pixels optimize the trade-off between uncertainty and dynamic range. In our field measurements, seeding density and droplet size cannot be controlled, necessitating a compromise between measurement accuracy in measuring displacement (favouring larger interrogation windows) and the resolution needed to capture small-scale turbulent velocity fluctuations close the Kolmogorov scales (favouring smaller interrogation windows).

To find the optimal vector spacing for 2D PIV from field measurements, for which a ground-truth references does not exist, the mean energy dissipation rate from the 1D structure function is compared to the mean energy dissipation rate from 2D gradient methods (Fig. 11). Since both energy dissipation rates are estimated from the same PIV-measured flow, albeit

https://doi.org/10.5194/egusphere-2026-3456
Preprint. Discussion started: 1 July 2026


at different effective sampling frequencies, their mean values should be similar if systematic biases are properly mitigated (e.g. see Figure 6 in Schröder et al. (2024)). Our velocity bias corrections establishes a linear relationship between the two methods, with the closest match at a vector spacing of 32 pixels (about 3 mm) across multiple EUREC$^4$A datasets. This spacing corresponds to roughly 3–6 times the Kolmogorov length scale, similar to the 4 mm laser sheet thickness. Note that at three times the Kolmogorov scale, localized dissipation can be underestimated by up to 60% (Tanaka and Eaton, 2007). Based on the post-processing methods and conservative filters applied here to exclude invalid or inaccurate interrogation windows, the displacement uncertainty in the PIV measurements is estimated to be up to 0.05 pixels (i.e., about 0.05 m/s in our setup) (Raffel et al., 2018; Michaelis et al., 2016). To further assess error propagation, Monte Carlo simulations were performed. The results indicate that a displacement uncertainty of 0.05 pixels leads to a mean error of approximately 48 % in the estimated energy dissipation rate. In comparison, the frame-to-frame variability of the original 2D PIV estimates spans approximately one order of magnitude (max/min $\approx$ 10). Overall, the airborne 2D PIV measurements of the MPCK$^+$, combined with the post-processing methods described above, provide reliable time-resolved estimates of the turbulence kinetic energy dissipation rate. The agreement between mean dissipation rates derived from 2D and 1D PIV indicates that the applied post-processing methods, including velocity bias removal, are valid and consistent with Monte Carlo uncertainty estimates. The resulting values remain within the uncertainty ranges expected based on literature guidelines, despite being obtained in an airborne configuration under uncontrolled in-cloud conditions.

### 7.5 Detection threshold and size-dependent sensitivity of PIV measurements

To estimate the PIV detection threshold as a function of droplet size, we first compare PIV measurements with FCDP using statistical correlation analyses. FCDP detects particles with diameters down to 1.5 µm and operates continuously throughout the flight with long operational overlap with PIV. Using it as a first step maintains independence from holography and enables a subsequent independent cross-check of holographic measurements against PIV. As noted above and shown in Figure 10, the PIV detection efficiency varies across the image, with the minimum detectable droplet size increasing from left to right due to beam divergence and changing scattering geometry. To quantify this effect, we divide the PIV image into vertically centred subregions (100 pixels high by 150 pixels wide) and systematically shift these subregions from left to right to sample different scattering and detection regimes. For each subregion, the total droplet count (after background removal and local maxima detection of particle blobs) is compared with particle-resolved FCDP measurements (i.e. so called particle-by-particle data) using varying minimum diameter thresholds over the corresponding PIV sampling interval (1/15 s). Each combination of PIV subregion and FCDP diameter cut-off defines a dataset, which is then aggregated across both day and night flights to account for variations in illumination conditions.

In the case of perfect agreement, where the effective detection threshold of the cropped PIV subregion matches the minimum droplet diameter cut-off applied to the FCDP data, a Pearson correlation coefficient of 1.0 and a fitted-line slope of 1.0 are expected when regressing PIV counts on FCDP counts. Lower correlation indicates a threshold mismatch, while slopes smaller (larger) than 1.0 indicate that FCDP measures higher (lower) concentrations than PIV. These analyses are meaningful when aggregating as much data as possible to characterize PIV's systematic behaviour assuming that the aggregated FCDP

https://doi.org/10.5194/egusphere-2026-3456
Preprint. Discussion started: 1 July 2026


dataset is free of systematic bias. As shown later, the FCDP exhibits limitations during the EUREC$^4$A flights, particularly in underdetecting large particles. These issues primarily affect absolute concentrations and seem to be concerning detection of drops >15 µm in diameter, whereas cross-instrument correlations remain high. Therefore, when inferring the PIV detection threshold from FCDP measurements, we rely on aggregated statistics and place greater confidence in droplet diameter cut-off thresholds well below 15 µm, where sufficient data points are still available. We also assume, as a first-order approximation, that the detection efficiency varies linearly as the crop moves from forward- to backward-scattering regions (left to right). While there is a general tendency for reduced detection of small particles toward backward scattering, this assumption is not strictly valid, as Mie scattering exhibits strong angular variability around 90°.

Table 4 summarizes FCDP-PIV intercomparison results, reporting the FCDP cut-off sizes that yield slopes closest to unity for each cropped PIV region. The corresponding correlation coefficients are also listed and are, in almost all cases, the highest—or near-highest—among the examined cut-off diameters. As expected, the minimum detectable or cut-off diameter increases as the crop moves from left to right across the image, reflecting the transition from forward to backward scattering. Unexpectedly, the FCDP cut-off corresponding to a given PIV crop is lower for day flights than for night flights, despite higher background intensity during the day that would be expected to reduce sensitivity to small droplets. A likely explanation is sampling: the daytime dataset is about an order of magnitude smaller, and the clouds encountered during these flights were dominated by small droplets, limiting robust correlations with larger diameter thresholds. Overall, given the relatively low correlations for some crops, the simplifying assumptions outlined above, and known limitations (e.g. FCDP detection biases and day–night differences), these results should be interpreted with caution and primarily as qualitative guidance. The PIV-FCDP intercomparison suggests that PIV can detect particles as small as ∼1.5 µm near the left edge (forward-scattering region), while toward the right edge (backward-scattering region) the effective detection limit increases to ∼4–8 µm. The latter range can be independently assessed using holography, as shown below.

| | Center of the selected region in PIV image (pixels) | | | | | | | | | | | |
|---|---|---|---|---|---|---|---|---|---|---|---|---|
| | 50 | 150 | 250 | 350 | 450 | 550 | 650 | 750 | 850 | 950 | 1050 | 1150 |
| Day flight | **>1.5 µm** (1.2, 0.7) | **>1.5 µm** (1.2, 0.6) | **>1.5 µm** (1.2, 0.6) | **>1.5 µm** (1.1, 0.6) | **>1.5 µm** (1.1, 0.6) | **>1.5 µm** (1.0, 0.6) | **>1.5 µm** (1.0, 0.5) | **>1.5 µm** (1.0, 0.6) | **>3.0 µm** (1.2, 0.4) | **>3.0 µm** (1.1, 0.4) | **>3.0 µm** (1.1, 0.3) | **>4.5 µm** (1.3, 0.4) |
| Night flight | **>1.5 µm** (1.2, 0.6) | **>1.5 µm** (1.1, 0.6) | **>1.5 µm** (1.0, 0.6) | **>3.0 µm** (1.1, 0.6) | **>3.0 µm** (1.0, 0.6) | **>4.5 µm** (1.1, 0.6) | **>4.5 µm** (1.0, 0.5) | **>6.0 µm** (1.1, 0.5) | **>6.0 µm** (1.0, 0.5) | **>6.0 µm** (0.9, 0.4) | **>8.0 µm** (1.2, 0.3) | **>8.0 µm** (1.1, 0.3) |

**Table 4.** Comparison of PIV-detected particle counts with FCDP measurements across different regions of the PIV image. Each column corresponds to a 100 × 150 pixel subregion, with its centre position indicated at the top (from left: forward scattering, to right: backward scattering). For each subregion, PIV counts are compared with FCDP counts above a minimum droplet diameter (bold, in µm). Each cell reports this cut-off diameter, followed by the slope and $R^2$ of a linear fit between PIV and FCDP counts (in parentheses). Results are shown separately for day and night flights during EUREC$^4$A (1779 and 19377 samples, respectively). All data shown in this table are based on images acquired with the first PIV laser head, which operates at slightly lower pulse energy and thus represents the minimum detection efficiency of the PIV system.

https://doi.org/10.5194/egusphere-2026-3456
Preprint. Discussion started: 1 July 2026


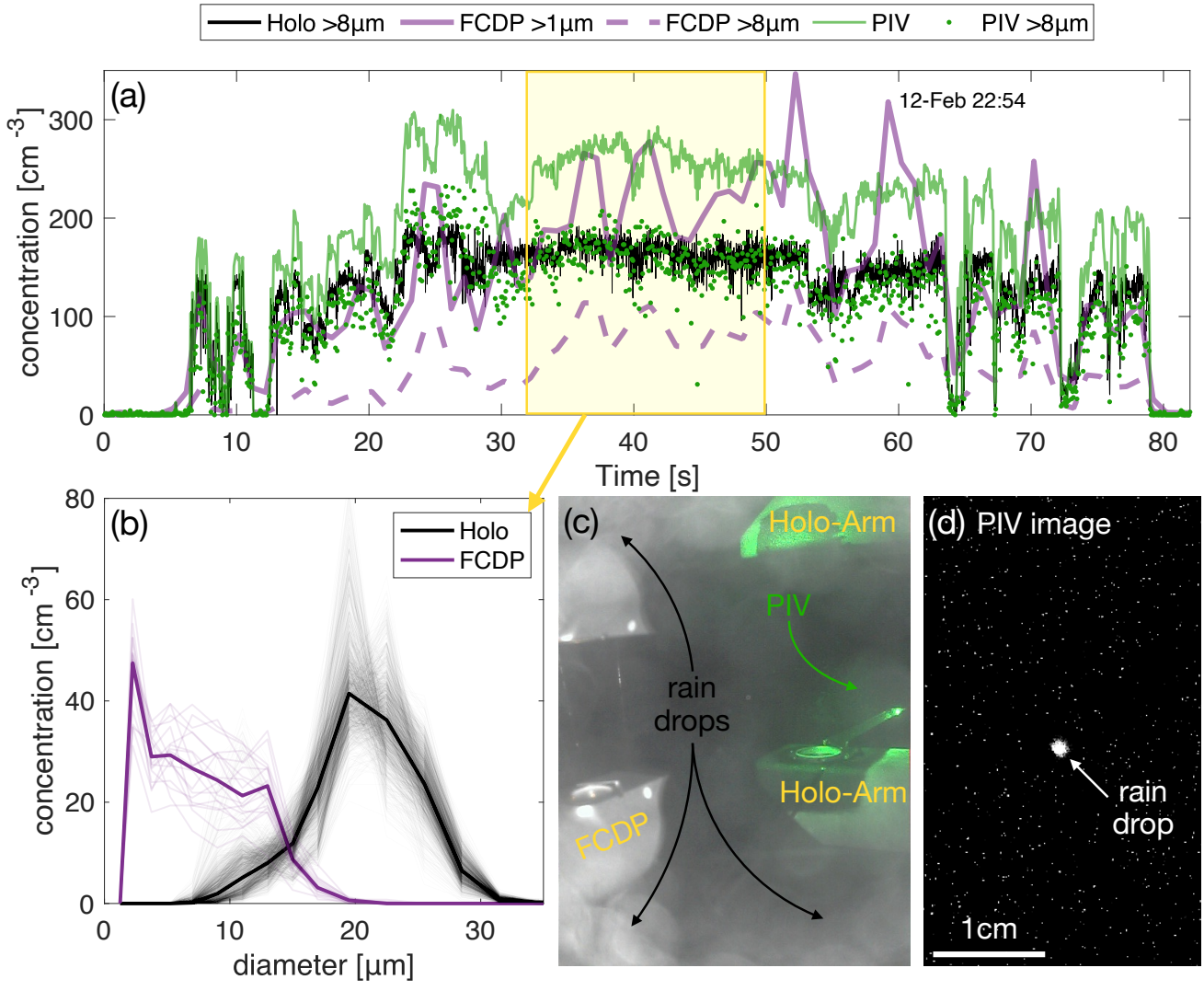


**Figure 12.** (a) Comparison of total concentration profile for a 80 s path through a precipitating cloud. Holographic and FCDP concentration can be directly conditioned on particle size, while for PIV the minimum cutoff can be chosen by choosing the right region (see Table 4). (b) Comparison of size distributions measured with FCDP and Holography within the section marked in yellow in (a). Individual lines show size distributions per hologram/ per 1s of FCDP measurement and bold line shows the median. (c) Flight camera image shows rain droplets on windows and rain droplets can also be identified in PIV images (d) which confirms precipitation of the cloud.

### 7.6 Comparison between holography, PIV and FCDP

From the droplet measurements of the holographic system, PIV setup, and FCDP, the droplet number concentration can be determined. To assess their consistency, measurements from the three instruments are compared. Figure 12 (a) shows the

https://doi.org/10.5194/egusphere-2026-3456
Preprint. Discussion started: 1 July 2026


concentration profile along a horizontal flight segment through a cloud (approximately 80 s ≈ 1 km). For PIV and holography the concentration is calculated per frame and for FCDP for every second of measured data. Counting all droplets measured by FCDP and PIV compared to holography, where only droplets larger than 8 µm are counted as valid, shows the same overall trends but higher concentration as PIV and FCDP are sensitive also to particles down to 1-1.5 µm. As discussed in Section 7.5, the minimum detectable diameter for PIV varies with the selected subregion. When PIV concentrations are restricted to droplets $> 8$ µm, by evaluating only the subregions with minimum detectable diameter 8 µm , the profile aligns remarkably well with holography, confirming the validity of both systems and the PIV subregion cut-off diameter determination approach outlined in Section 7.5. However, when comparing only droplets $> 8$ µm, FCDP-derived concentrations are significantly lower than those from holography and PIV. The mismatch is further evident in the size distributions: in the constant concentration region marked in light yellow in Figure 12(a), holography captures a mean droplet diameter of $\sim 20$ µm with a pronounced left tail, consistent with reliable detection above 8 µm. In contrast, FCDP reports a nearly uniform distribution below 15 µm with no droplets above 20 µm as shown in Figure 12(b). This inconsistency persists across multiple sections in flights 6 and 12 of the EUREC$^4$A campaign. This discrepancy may arise from either reduced detection efficiency for larger droplets in the FCDP or a systematic sizing bias causing larger droplets to be misclassified into smaller size bins but the exact reason remains unclear. Notably, in the subsequent PaCE 2022 campaign, FCDP and holography size distributions show excellent agreement (see Schlenczek et al. (2025), Figure 9). Given that our holographic system and processing algorithms have been extensively validated with quantified uncertainties, it is likely that the FCDP exhibited operational issues during the EUREC$^4$A campaign. This is particularly plausible since larger droplets are expected in precipitating clouds, as in the example shown. Precipitation is clearly determined through rain drops visible via the flight camera and in PIV images (Fig. 12(c) and (d)). Although the FCDP was operated outside its nominal velocity range (10–200 m/s) on the MPCK$^+$, this condition also occurred during PACE 2022 without similar discrepancies, suggesting that velocity is not the primary cause. Thus, the observed divergence during EUREC$^4$A likely reflects instrument-specific anomalies rather than fundamental measurement limitations.

Figure 13 shows examples of the measurement capabilities of the MPCK$^+$ instrument, where the holographic volume is acquired simultaneously with the first PIV image. As a reminder, the gravity direction is parallel to the hologram sampling volume. For these plots, a central slice of width 4 mm through the three-dimensional holographic volume is overlaid on the PIV image. Small mismatches are expected due to slight deviations between the holographic volume and the quasi-two-dimensional PIV sheet, as well as differences in droplet detection thresholds, and therefore a one-to-one correspondence between droplets is not expected.

In the left panel, when droplet diameters are close to the detection limit of the holographic system (Nyquist criterion of 2 pixels or 6 µm), they are not reliably detected in the holograms, while many remain clearly visible in the PIV image. Together with the results presented in Table 4 and Figure 12, this confirms that the detection limit of the PIV system is below 6 µm, even during daytime flights where sunlight increases background noise and reduces particle detectability in PIV images. In the middle panel, where most droplets exceed the holographic detection limit, similar entrainment and mixing structures are observed in both PIV and holographic data, supporting the reliability of holographic classification and sizing. In the right panel, where droplet diameters are well above the holographic detection threshold, a large number of droplets within the cloud core

https://doi.org/10.5194/egusphere-2026-3456
Preprint. Discussion started: 1 July 2026


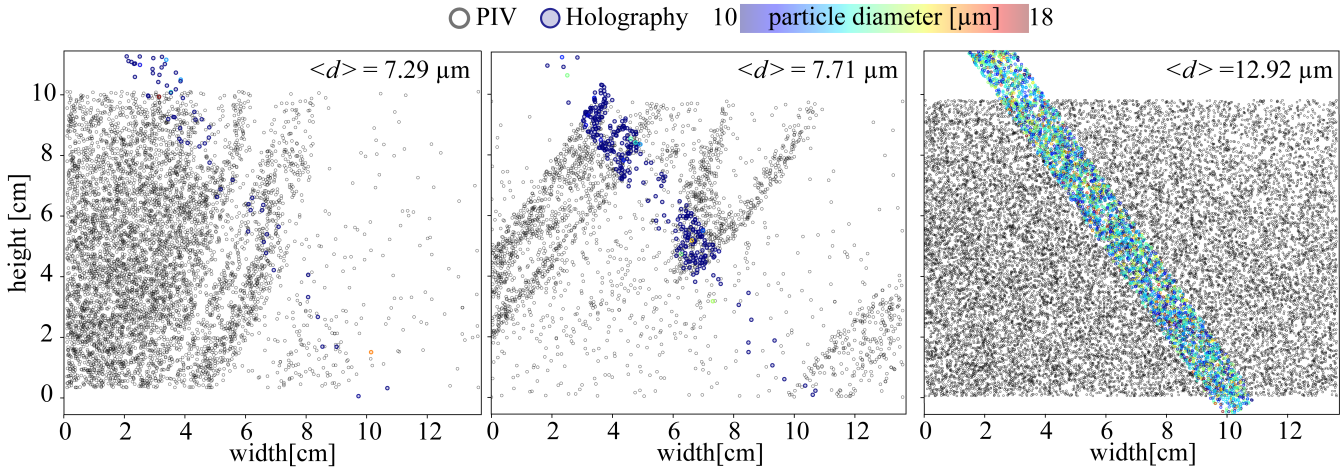


**Figure 13.** PIV images overlaid with co-located 4 mm central slices of simultaneously acquired holograms during a daytime flight (Flight 6) of the EUREC$^4$A field campaign on 4 February 2020, showing a diluted cloud edge (left), a less-diluted cloud edge (centre), and a cloud core located approximately 200 m from the nearest lateral cloud boundary (right). The mean diameter $\langle d \rangle$ shown above each sub-plot is computed from droplets detectable by the holographic system within the corresponding hologram. Each circular symbol represents an individual cloud droplet measured by the PIV (black) and holographic (size-coloured) systems.

are detected with both imaging systems, and zoomed views reveal agreement in small-scale structures, such as voids, between the PIV image and holographic reconstruction. These unique co-located and simultaneous measurements are highly valuable for unravelling the interaction between localised cloud microphysics and turbulence, while providing a powerful framework for data quality control, redundancy, and robust assessment of holographic analysis performance.

### 7.7 The turbulent kinetic energy dissipation rate

Most, if not all, airborne estimates of the turbulent kinetic energy dissipation rate, $\epsilon$, have relied on anemometers, typically invoking Taylor's frozen-turbulence hypothesis together with assumptions of statistical stationarity, homogeneity, and isotropy. Owing to limited spatiotemporal resolution, these methods usually infer $\epsilon$ from one-dimensional surrogates (e.g., inertial-range statistics of the longitudinal velocity). Accuracy is sensitive to several factors, including angle of attack, averaging-window length, turbulence intensity, dominant platform oscillations, and variable heading (e.g. see Schröder et al., 2024, and references therein). Among these, the averaging window is particularly critical: a 50% deviation from the true global mean $\epsilon$ can persist unless the window spans at least $\sim$10 integral length scales (i.e., $\mathcal{O}(1\text{–}10)$ km in the atmosphere, see Schröder et al., 2024). By contrast, two-frame PIV provides frame-by-frame $\epsilon$ estimates from spatial velocity gradients within the illuminated sheet, reducing sensitivity to platform motion and providing the possibility to measure instantaneous $\epsilon$.

Figure 14 compares dissipation rates from 1D and 3D pitot tubes, as well as 1D and 2D PIV across three flights. Here, we analyse the effect of averaging on the dissipation rate by adding dissipation rates estimated from the moving-averaged 3D pitot tube data, because the 1D pitot tube always averaged over eight points. On 28 January (keel-mount, subset of Flight 3), the 1D

https://doi.org/10.5194/egusphere-2026-3456
Preprint. Discussion started: 1 July 2026


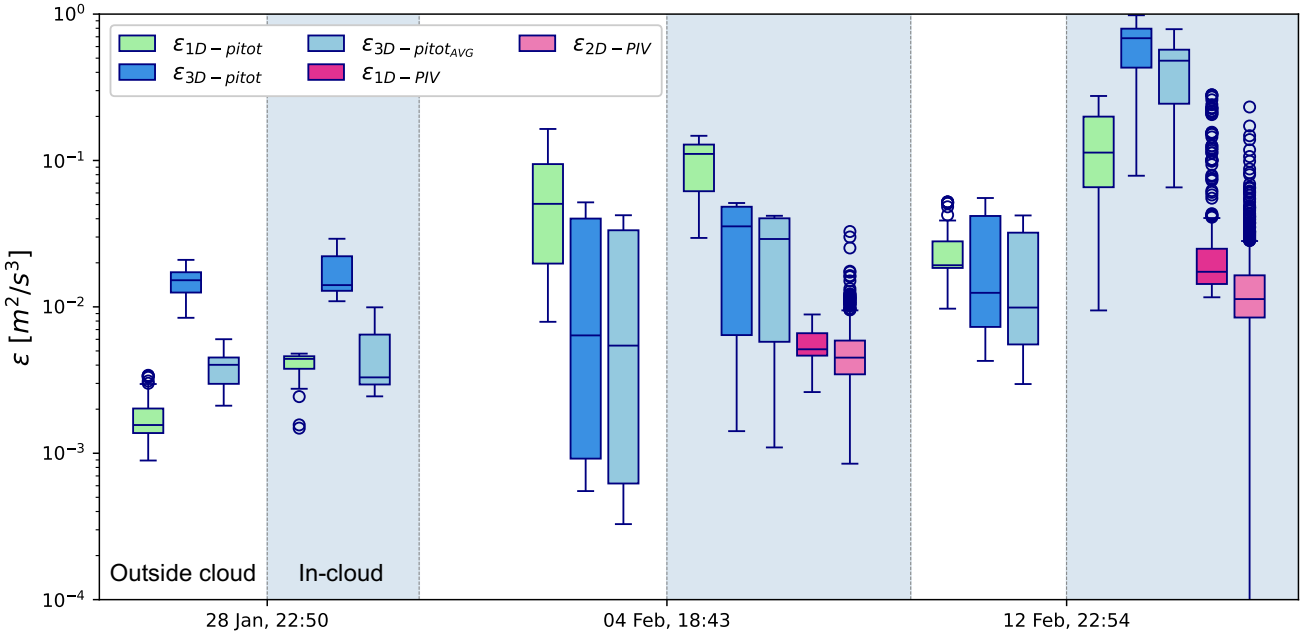


**Figure 14.** Distribution of the energy dissipation rates, $\epsilon$, measured by different sensors of MPCK$^+$ instrument across multiple flights, mounting methods and weather conditions. $\epsilon_{\text{3D-Pitot}_{\text{AVG}}}$ is calculated from the moving average of 3D pitot tube data using a window size of 8. The 1D and 2D PIV methods are follow those described in 7.4. The shaded region indicates the dissipation rate measured inside the clouds; unshaded areas represent the free atmosphere.

pitot tube shows rates 10 times lower than the 3D pitot tube, illustrating the effect of averaging, explaining by the averaged 3D data yield 7 times lower dissipation than the original. Figure 15a shows a similar effect in the structure function, with the averaged 3D data shifted downward and steeper on small scales, resembling the 1D pitot results.

For the spar-mount flights (4 and 12 February), platform instability increased fluctuations in 1D and 3D pitot dissipation rates. On 4 February, the 1D pitot tube overestimates dissipation due to direct platform-induced energy injection (see Figure 7b), with structure functions exceeding other sensors by up to a factor of six (Fig. 15b). On 12 February, rain clogged the pitot tubes, causing large signal fluctuations and unrealistically high dissipation rates. Interestingly, despite the mounting methods used, the dissipation rates inside the cloud (shaded region in Figure 14) are higher than in the free atmosphere on all flights.

Overall, PIV provides robust dissipation rate estimates across different mount methods and weather conditions. The 2D PIV shows a broader range of dissipation rates than the 1D PIV due to its higher temporal resolution, whereas the 1D PIV requires averaging over approximately 30 s (see Figure 6 in Schröder et al., 2024). These results further highlight the strong capability of PIV compared to other sensors for in-cloud turbulence measurements.

https://doi.org/10.5194/egusphere-2026-3456
Preprint. Discussion started: 1 July 2026


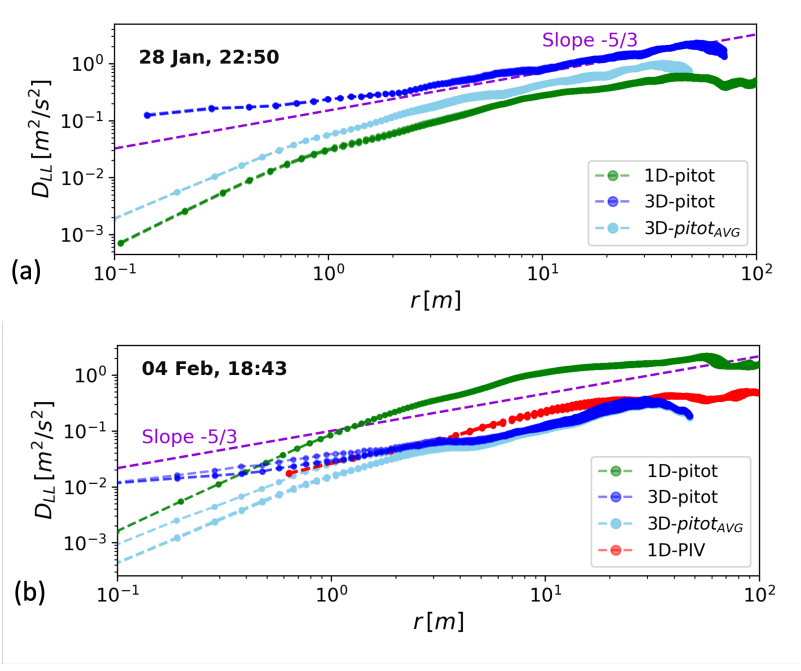


**Figure 15.** The second order structure function calculated using different measurement methods along to the length scale at (a) Jan 28, 22:50 (subset of Flight 3) and (b) Feb 04, 18:43 (subset of Flight 6).

## 8 Conclusions

We have introduced the airborne Max Planck CloudKite platform and one of the first scientific instruments developed for it, i.e. the MPCK$^+$ instrument. The MPCK platform is designed to probe the atmospheric boundary layer and clouds within 2 km AGL. Its key advantages include low true airspeed, multi-altitude sampling, and prolonged operation, enabling observations over periods ranging from hours to multiple diurnal cycles, depending on the power and data-storage capacity of the scientific payload. The MPCK$^+$ instrument is designed to provide high-cadence measurements of localised cloud microphysics and turbulence. The aim is to shed light on small-scale processes from cloud edge to core and provide insights into entrainment/mixing, the role of turbulence, and the mechanisms of precipitation. We demonstrate that deploying instruments such as MPCK$^+$ instrument on the MPCK platform is feasible and enables unique scientific measurements, including advanced airborne imaging (PIV and holography). Using data from field campaigns combined with laboratory measurements, the reliability of the platform and MPCK$^+$ instrument are assessed. Various mounting possibilities are discussed and their flight stability performance are quantified. The best overall mounting strategy is the on-tether mounting method, followed by the keel mount and then the spar mount.

The MPCK$^+$ performance during in-situ measurements are comprehensively evaluated, specifically temperature, relative humidity, velocity, and cloud microphysics. Relative humidity and temperature agreed closely with radiosondes in cloud-

https://doi.org/10.5194/egusphere-2026-3456
Preprint. Discussion started: 1 July 2026


free conditions, whereas in-cloud performance was less reliable and requires further improvement. All velocity measurements required correction due to the disturbance caused by the external geometry of MPCK$^+$. Through wind-tunnel calibrations, these corrections are validated and have been shown to be reliably applicable. Velocity measurements from pitot tubes generally agreed with each other and with PIV, with caveats related to in-cloud conditions and being sensitive to mounting method for characterizing turbulence features.

PIV performed robustly across a wide range of cloud conditions, including intense precipitation, enabling direct in-situ measurements of turbulent velocity field structure and energy dissipation rates within clouds at unprecedented spatiotemporal resolution. In addition, the measurements provided a valuable framework for quantifying aerodynamic disturbances induced by the holographic arms, evaluating pitot-tube performance, and cross-validating observations with FCDP and holography. Furthermore, velocity measurements made by the PIV system showed low correlation with platform angular oscillations, which is essential for reliable measurements on a passively controlled airborne platform such as MPCK$^+$. PIV performance for measuring the turbulence kinetic energy dissipation rate, as one of the key parameters for characterizing turbulence, was thoroughly evaluated. We presented in-situ analysis methods and detailed necessary corrections, and compared results with pitot tubes as well as PIV approaches (1D versus 2D). Collectively, the agreement with pitot tubes, the consistency between 1D and 2D PIV, and the established capabilities of PIV measurement principles indicate that the dissipation rate can be measured reliably with MPCK$^+$. Given the inherent challenges of turbulence characterisation with conventional anemometers (Schröder et al., 2024), this capability represents a major observational advance enabled by the MPCK$^+$ instrument, providing a new pathway for investigating turbulence–microphysics interactions at centimetre scales throughout clouds.

The MPCK$^+$ holographic system operated reliably throughout airborne deployments, providing localised droplet size distributions at unprecedented spatial sampling resolution, with hologram spacing as low as a few centimetres. Its co-location with the PIV sampling volume enabled both rigorous assessment of holographic performance and a unique opportunity to directly investigate links between cloud microphysics and local turbulence in natural clouds. We conducted in-lab characterisation of the holographic setup and, together with prior work using this system (Thiede et al., 2025c), demonstrated that MPCK$^+$ has a nominal detection limit of 6 µm and reliably detects and sizes droplets larger than 8 µm within the sample volume. The sizing and detection efficiencies depend on particle size and position within the volume, as discussed in detail by Thiede et al. (2025c). Here, we further extend this characterisation with additional laboratory calibration, including particle shape detection, and in-situ performance assessment through intercomparisons with FCDP and PIV.

Across cloud events, FCDP, PIV, and holography generally agree closely on event timing and the shapes of concentration curves, yet quantitative differences remain. Some discrepancies are attributable to differing detection efficiencies. For example, PIV consistently reports higher total droplet number concentrations than holography because PIV detects smaller particles. We calibrated different regions of the PIV image to estimate the lower detection cut-off size as a function of droplet position in the PIV beam, using correlations with aggregated FCDP data. With this approach, PIV and holography show very good agreement on absolute concentrations for droplets larger than 8 µm in individual cloud events. During the EUREC$^4$A campaign, FCDP showed difficulties capturing concentrations of large particles, especially those larger than 15 µm. However, we do not consider

https://doi.org/10.5194/egusphere-2026-3456
Preprint. Discussion started: 1 July 2026


this an inherent limitation of FCDP or a consequence of the low TAS of the MPCK platform; in another field campaign Schlenczek et al. (2025), FCDP exhibited close agreement with MPCK$^+$ holography even at at lower TAS.

Overall, we conclude that the CloudKite platform, together with the MPCK$^+$ instrument, has now been quantitatively characterized. While there remains room for further improvement, the major design objectives, e.g. stable and reliable operation, and localised high-cadence turbulence and microphysics measurements, have been successfully demonstrated. These results establish MPCK platform and MPCK$^+$ as a capable and versatile platform and instrument for probing small-scale processes in clouds and the atmospheric boundary layer, and they provide a solid foundation for future developments.

*Code and data availability.* Not applicable: this study reports instrument design, calibration, analysis procedures and performance evaluation only; no research datasets beyond examples were generated.

*Author contributions.* GB and EB conceptualised the MPCK platform. GB and FN conceptualised the MPCK$^+$ instrument, and GB developed its initial design. GB, FN, PH, TN, and OS built the first version of MPCK$^+$ and developed the operating software. GB, FN, OS, YK, and EB contributed to subsequent refinements of the instrument. GB, FN, BT, YK, VC, and OS contributed to data post-processing and preparation of the initial manuscript draft. All authors contributed to the final manuscript.

*Competing interests.* The authors declare no competing interests.

*Acknowledgements.* We thank the MPI-DS Machine Shop (lead by Udo Schminke and André Heil), the MPI-DS Electronics Workshop (in particular Laura Diaz and Holger Nobach), the institute technicians and engineer (Andreas Kopp, Andreas Renner, Marcel Meyer, Artur Kubitzek), and the MPI-DS HPC and IT personel (Denny Fliegner, Hecke Degering, and Gerhard Nolte) for their help and work with designing, building, testing, and improving the MPCK$^+$ and its support systems. We thank Andreas Kopp, Johannes Güttler, Kashawn Hall, Marcel Meyer, and Björn Stevens for being additional operators of the MPCK$^+$ repair, discussions, etc. on MSM82/2 and/or MSM89. We thank Antonio Ibáñez-Landeta for making the shape-determination calibration-mask for the holography system. We thank Guus Bertens for the idea to use `O_DIRECT` to reduce the overhead of writing the holography images to disk. We thank Raymond Shaw and Jacob Fugal for important discussions and feedback on the holography system during the design stage. We thank Jacob Fugal for discussion and recommendations on the choice of CDP. We thank Holger Siebert for discussions and guidance on flying tethered aerostats including airspace rules, discussing ACTOS and BELUGA, and showing us ACTOS. We thank Björn Stevens for the idea to fly from the RV Maria S Merian, scientific discussions, connecting us with EUREC$^4$A collaboration. We thank Allsopp Helikites and Skylaunch for training, customizing the balloons and winches for the project, and repair work. We thank the Leitstelle Deutsche Forschungs-Schiffe for all the information, logistics, guidance, and other assistance for safe operation of the CloudKite from their ships. We thank iw Machinenbau GmbH for verifying the designs of the A-frame mount, ground mount point, and handling winch mount for the RV Maria S Merian. We thank Ship Design & Consult GmbH for verifying the design of and finding the maximum safe line tensions for the A-frame mount for the RV Maria S Merian. We thank

https://doi.org/10.5194/egusphere-2026-3456
Preprint. Discussion started: 1 July 2026


the officers and crew of the RV Maria S Merian during voyages MSM82/2 and MSM89, particularly Captain Björn Maass (both voyages) and Bosuns Enno Vredenborg (MSM82/2) and Sebastian Plink (MSM89), for all of their guidance, assistance, finding ways to make things work, etc. We thank Ingenieurbüro Goebel GmbH for their help with improving the MPCK$^{+}$'s laser safety systems. We thank Bernd Rathmann GmbH and Krinner Schraubfundamente GmbH for their help with ground anchors. We thank Bernd Rathmann GmbH; LP Logistics; the crew of the RV Maria S Merian; and the ports of Montevideo, Las Palmas, and Bridgetown for all of their work and assistance with loading; unloading; and transport of the CloudKite and support systems. We thank the other members of the EUREC$^{4}$A-ATOMIC collaboration for helpful scientific and flight profile discussions in the planning stages before MSM82/2 and MSM89.

https://doi.org/10.5194/egusphere-2026-3456
Preprint. Discussion started: 1 July 2026


## References

Abdelmonem, A., Järvinen, E., Duft, D., Hirst, E., Vogt, S., Leisner, T., and Schnaiter, M.: PHIPS–HALO: The airborne particle habit imaging and polar scattering probe–Part 1: Design and operation, Atmospheric Measurement Techniques, 9, 3131–3144, 2016.

Allsopp Helikites Ltd: Helikite Aerostats: Helium Kites and Aerostats, https://www.helikites.com/, accessed: 1 December 2025.

Allwayin, N., Larsen, M. L., Glienke, S., and Shaw, R. A.: Locally narrow droplet size distributions are ubiquitous in stratocumulus clouds, Science, 384, 528–532, 2024.

Bagheri, G., Schlenczek, O., Turco, L., Thiede, B., Stieger, K., Kosub, J.-M., Pöhlker, M. L., Pöhlker, C., Moláček, J., Scheithauer, S., and Bodenschatz, E.: Exhaled particles from nanometre to millimetre and their origin in the human respiratory tract, medRxiv, https://doi.org/10.1101/2021.10.01.21264333, 2021.

Balsley, B. B., Williams, J., Tyrrell, G., and Balsley, C.: Atmospheric research using kites: Here we go again!, Bulletin of the American Meteorological Society, 73, 17–30, 1992.

Balsley, B. B., Jensen, M. L., and Frehlich, R. G.: The use of state-of-the-art kites for profiling the lower atmosphere, Boundary-Layer Meteorology, 87, 1–25, 1998.

Baumgardner, D., Abel, S. J., Axisa, D., Cotton, R., Crosier, J., Field, P., Gurganus, C., Heymsfield, A., Korolev, A., Krämer, M., Lawson, P., McFarquhar, G., Ulanowski, Z., and Um, J.: Cloud Ice Properties: In Situ Measurement Challenges, Meteorological Monographs, 58, 9.1–9.23, https://doi.org/10.1175/amsmonographs-d-16-0011.1, 2017.

Beals, M. J.: Investigations of Cloud Microphysical Response to Mixing Using Digital Holography, Ph.D. thesis, Michigan Technological University, ISBN 9781303736155, http://digitalcommons.mtu.edu/etds/669, 2013.

Beals, M. J., Fugal, J. P., Shaw, R. A., Lu, J., Spuler, S. M., and Stith, J. L.: Holographic measurements of inhomogeneous cloud mixing at the centimeter scale, Science, 350, 87–90, https://doi.org/10.1126/science.aab0751, 2015.

Bodenschatz, E., Malinowski, S. P., Shaw, R. A., and Stratmann, F.: Can We Understand Clouds Without Turbulence?, Science, 327, 970–971, https://doi.org/10.1126/science.1185138, 2010.

Chávez-Medina, V., Khodamoradi, H., Schlenczek, O., Nordsiek, F., Brunner, C. E., Bodenschatz, E., and Bagheri, G.: Max Planck WinDarts: High-Resolution Atmospheric Boundary Layer Measurements with the Max Planck CloudKite platform and Ground Weather Station–A Data Overview, Earth System Science Data Discussions, 2025, 1–22, 2025.

Conover, J. H.: Atmospheric Sounding by Kites and Other Kite Experiments: 1894–1904, pp. 67–106, American Meteorological Society, Boston, MA, ISBN 978-1-940033-82-2, https://doi.org/10.1007/978-1-940033-82-2_6, 1990.

Creamean, J. M., Dexheimer, D., Hume, C. C., Vazquez, M., Hess, B. T. M., Longbottom, C. M., Ruiz, C. A., and Theisen, A. K.: Reaching new heights: A vertically-resolved ice nucleating particle sampler operating on Atmospheric Radiation Measurement (ARM) tethered balloon systems, https://doi.org/10.5194/egusphere-2025-5000, 2025.

Devenish, B., Bartello, P., Brenguier, J.-L., Collins, L., Grabowski, W. W., IJzermans, R., Malinowski, S. P., Reeks, M., Vassilicos, J., Wang, L.-P., et al.: Droplet growth in warm turbulent clouds, Quarterly Journal of the Royal Meteorological Society, 138, 1401–1429, 2012.

Doron, P., Bertuccioli, L., Katz, J., and Osborn, T.: Turbulence characteristics and dissipation estimates in the coastal ocean bottom boundary layer from PIV data, Journal of Physical Oceanography, 31, 2108–2134, 2001.

Egerer, U., Gottschalk, M., Siebert, H., Ehrlich, A., and Wendisch, M.: The new BELUGA setup for collocated turbulence and radiation measurements using a tethered balloon: first applications in the cloudy Arctic boundary layer, Atmospheric Measurement Techniques, 12, 4019–4038, https://doi.org/10.5194/amt-12-4019-2019, 2019.

https://doi.org/10.5194/egusphere-2026-3456
Preprint. Discussion started: 1 July 2026


Fuchs, C., Ramelli, F., Schweizer, D., Lohmann, U., and Henneberger, J.: Putting the spotlight on small cloud droplets with SmHOLIMO - a new holographic imager for in situ measurements of clouds, Atmospheric Measurement Techniques, 18, 2969–2986, https://doi.org/10.5194/amt-18-2969-2025, 2025.

Fugal, J. and Shaw, R.: Cloud particle size distributions measured with an airborne digital in-line holographic instrument, Atmospheric Measurement Techniques, 2, 259–271, 2009a.

Fugal, J. P. and Shaw, R. A.: Cloud particle size distributions measured with an airborne digital in-line holographic instrument, Atmospheric Measurement Techniques, 2, 259–271, https://doi.org/10.5194/amt-2-259-2009, 2009b.

Fugal, J. P., Schulz, T. J., and Shaw, R. A.: Practical methods for automated reconstruction and characterization of particles in digital in-line holograms, Measurement Science and Technology, 20, 075501, https://doi.org/10.1088/0957-0233/20/7/075501, 2009.

George, W. K. and Hussein, H. J.: Locally axisymmetric turbulence, Journal of Fluid Mechanics, 233, 1–23, 1991.

Glienke, S., Kostinski, A. B., Shaw, R. A., Larsen, M. L., Fugal, J. P., Schlenczek, O., and Borrmann, S.: Holographic Observations of Centimeter-Scale Nonuniformities within Marine Stratocumulus Clouds, Journal of Atmospheric Sciences, 77, 499–512, https://doi.org/10.1175/JAS-D-19-0164.1, 2020.

Grabowski, W. W. and Wang, L.-P.: Growth of cloud droplets in a turbulent environment, Annual review of fluid mechanics, 45, 293–324, 2013.

Greenspan, L.: Humidity Fixed Points of Binary Saturated Aqueous Solutions, Journal of Research of the National Bureau of Standards – A. Physics and Chemistry, 81A, https://doi.org/10.6028/jres.081A.011, 1977.

Henneberger, J., Fugal, J. P., Stetzer, O., and Lohmann, U.: HOLIMO II: a digital holographic instrument for ground-based in situ observations of microphysical properties of mixed-phase clouds, Atmospheric Measurement Techniques, 6, 2975–2987, 2013.

Henneberger, J., Ramelli, F., Spirig, R., Omanovic, N., Miller, A. J., Fuchs, C., Zhang, H., Bühl, J., Hervo, M., Kanji, Z. A., Ohneiser, K., Radenz, M., Rösch, M., Seifert, P., and Lohmann, U.: Seeding of Supercooled Low Stratus Clouds with a UAV to Study Microphysical Ice Processes: An Introduction to the CLOUDLAB Project, Bulletin of the American Meteorological Society, 104, E1962–E1979, https://doi.org/10.1175/BAMS-D-22-0178.1, 2023.

Heymsfield, A. J. and McFarquhar, G. M.: High albedos of cirrus in the tropical Pacific warm pool: Microphysical interpretations from CEPEX and from Kwajalein, Marshall Islands, Journal of Atmospheric Sciences, 53, 2424–2451, 1996.

Holtzer, G. L. and Collins, L. R.: Relationship between the intrinsic radial distribution function for an isotropic field of particles and lower-dimensional measurements, Journal of Fluid Mechanics, 459, 93–102, https://doi.org/10.1017/S0022112002008169, 2002.

Höhne, P.: Cloud Microphysics in Airborne and Laboratory Investigations, Master's thesis, Georg-August-Universität Göttingen, 2019.

Intergovernmental Panel on Climate Change: The Earth's Energy Budget, Climate Feedbacks and Climate Sensitivity, in: Climate Change 2021: The Physical Science Basis, pp. 923–1054, Cambridge University Press, https://doi.org/10.1017/9781009157896.009, 2021.

Karstensen, J., Lavik, G., Acquistapace, C., Bagheri, G., Begler, C., Bendinger, A., Bodenschatz, E., Böck, T., Güttler, J., Hall, K., Körner, M., Kopp, A., Lange, D., Mehlmann, M., Nordsiek, F., Reus, K., Ribbe, J., Philippi, M., Piosek, S., Ritschel, M., Tschitschko, B., and Wiskandt, J.: EUREC4A Campaign, Cruise No. MSM89, 17. January - 20. February 2020, Bridgetown $Barbados$ - Bridgetown $Barbados$, The ocean mesoscale component in the EUREC4A++ field study, MARIA S. MERIAN-Berichte, https://doi.org/10.2312/cr_msm89, 2020.

Korolev, A. and Milbrandt, J.: How Are Mixed-Phase Clouds Mixed?, Geophysical Research Letters, 49, e2022GL099 578, https://doi.org/10.1029/2022GL099578, e2022GL099578 2022GL099578, 2022.

https://doi.org/10.5194/egusphere-2026-3456
Preprint. Discussion started: 1 July 2026


Korolev, A., McFarquhar, G., Field, P. R., Franklin, C., Lawson, P., Wang, Z., Williams, E., Abel, S. J., Axisa, D., Borrmann, S., Crosier, J., Fugal, J., Krämer, M., Lohmann, U., Schlenczek, O., Schnaiter, M., and Wendisch, M.: Mixed-Phase Clouds: Progress and Challenges, Meteorological Monographs, 58, 5.1 – 5.50, https://doi.org/10.1175/AMSMONOGRAPHS-D-17-0001.1, 2017.

Korolev, A., McFarquhar, G., Field, P. R., Franklin, C., Lawson, P., Wang, Z., Williams, E., Abel, S. J., Axisa, D., Borrmann, S., Crosier, J., Fugal, J., Krämer, M., Lohmann, U., Schlenczek, O., Schnaiter, M., and Wendisch, M.: Mixed-Phase Clouds: Progress and Challenges, Meteorological Monographs, 58, 5.1–5.50, https://doi.org/10.1175/AMSMONOGRAPHS-D-17-0001.1, 2017.

Krastel, S., Kinne, S., Nitsche, F., Ahlers, J., Bischof, S., Bodenschatz, E., Cremanns, M., Düring, A., Höhne, P., Jeuck, A., Lenz, K.-F., Meyer, M., Pereyra, N., Rachid, J., Schiwitza, S., Schlenczek, O., Schopenhauer, M., Schröder, M., Stevens, B., Tewes, S., Vietheer, C., and Wagner, T.: Morphology of the headwall area of the Sahara slide, NW-Africa, Measuring Over Ocean References, Mapping sequences to protists morphospecies from the Atlantic, Cruise No. MSM82/2, 26.04.19 - 14.05.19, Montevideo $Uruguay$ - Las Palmas $Spain$, MARIA S. MERIAN-Berichte, https://doi.org/10.2312/cr_msm82_2, 2019.

Larsen, M., Briner, C., and Boehner, P.: On the recovery of 3D spatial statistics of particles from 1D measurements: Implications for airborne instruments, Journal of Atmospheric and Oceanic Technology, 31, 2078–2087, https://doi.org/10.1175/JTECH-D-14-00004.1, 2014.

Lonardi, M., Pilz, C., Siebert, H., Ehrlich, A., and Wendisch, M.: Tethered balloon-borne measurements of terrestrial radiation during MOSAiC leg 4 in July 2020, https://doi.org/10.1594/PANGAEA.944200, 2022.

Lu, J., Shaw, R. A., and Yang, W.: Improved particle size estimation in digital holography via sign matched filtering, Optics Express, 20, 12 666, https://doi.org/10.1364/OE.20.012666, 2012.

McFarquhar, G. M., Baumgardner, D., Bansemer, A., Abel, S. J., Crosier, J., French, J., Rosenberg, P., Korolev, A., Schwarzoenboeck, A., Leroy, D., Um, J., Wu, W., Heymsfield, A. J., Twohy, C., Detwiler, A., Field, P., Neumann, A., Cotton, R., Axisa, D., and Dong, J.: Processing of Ice Cloud In Situ Data Collected by Bulk Water, Scattering, and Imaging Probes: Fundamentals, Uncertainties, and Efforts toward Consistency, Meteorological Monographs, 58, 11.1–11.33, https://doi.org/10.1175/amsmonographs-d-16-0007.1, 2017.

Michaelis, D., Neal, D. R., and Wieneke, B.: Peak-locking reduction for particle image velocimetry, Measurement Science and Technology, 27, 104 005, 2016.

Morrison, H., Boer, G. D., Feingold, G., Harrington, J., Shupe, M. D., and Sulia, K.: Resilience of persistent Arctic mixed-phase clouds, Nature Geoscience, 5, 11–17, https://doi.org/10.1038/ngeo1332, 2012.

Murphy, D. M. and Koop, T.: Review of the vapour pressures of ice and supercooled water for atmospheric applications, Quarterly Journal of the Royal Meteorological Society, 131, 1539–1565, https://doi.org/10.1256/qj.04.94, 2005.

Muschinski, A., Frehich, R., Jensen, M., Hugo, R., Hoff, A., Eaton, F., and Balsley, B.: Fine-scale measurements of turbulence in the lower troposphere: An intercomparison between a kite-and balloon-borne, and a helicopter-borne measurement system, Boundary-layer meteorology, 98, 219–250, 2001.

Pasquier, J. T., Henneberger, J., Ramelli, F., Lauber, A., David, R. O., Wieder, J., Carlsen, T., Gierens, R., Maturilli, M., and Lohmann, U.: Conditions favorable for secondary ice production in Arctic mixed-phase clouds, Atmospheric Chemistry and Physics, 22, 15 579–15 601, https://doi.org/10.5194/acp-22-15579-2022, 2022.

Pasquier, J. T., Henneberger, J., Korolev, A., Ramelli, F., Wieder, J., Lauber, A., Li, G., David, R. O., Carlsen, T., Gierens, R., Maturilli, M., and Lohmann, U.: Understanding the History of Two Complex Ice Crystal Habits Deduced From a Holographic Imager, Geophysical Research Letters, 50, https://doi.org/10.1029/2022GL100247, 2023.

Pisano, J., McKendry, I., Steyn, D., and Hastie, D.: Vertical nitrogen dioxide and ozone concentrations measured from a tethered balloon in the Lower Fraser Valley, Atmospheric Environment, 31, 2071–2078, 1997.

https://doi.org/10.5194/egusphere-2026-3456
Preprint. Discussion started: 1 July 2026


Pohorsky, R., Baccarini, A., Brett, N., Barret, B., Bekki, S., Pappaccogli, G., Dieudonné, E., Temime-Roussel, B., D'Anna, B., Cesler-Maloney, M., Donateo, A., Decesari, S., Law, K. S., Simpson, W. R., Fochesatto, J., Arnold, S. R., and Schmale, J.: In situ vertical observations of the layered structure of air pollution in a continental high-latitude urban boundary layer during winter, Atmospheric Chemistry and Physics, 25, 3687–3715, https://doi.org/10.5194/acp-25-3687-2025, 2025.

Pumir, A. and Wilkinson, M.: Collisional aggregation due to turbulence, Annual Review of Condensed Matter Physics, 7, 141–170, 2016.

Raffel, M., Willert, C. E., Scarano, F., Kähler, C. J., Wereley, S. T., and Kompenhans, J.: Particle image velocimetry: a practical guide, springer, 2018.

Ramelli, F., Beck, A., Henneberger, J., and Lohmann, U.: Using a holographic imager on a tethered balloon system for microphysical observations of boundary layer clouds, Atmospheric Measurement Techniques, 13, 925–939, 2020.

Ramelli, F., Henneberger, J., Fuchs, C., Miller, A. J., Omanovic, N., Spirig, R., Zhang, H., David, R. O., Ohneiser, K., Seifert, P., and Lohmann, U.: Repurposing weather modification for cloud research showcased by ice crystal growth, PNAS Nexus, 3, https://doi.org/10.1093/pnasnexus/pgae402, 2024.

Schlenczek, O.: Airborne and ground-based holographic measurement of hydrometeors in liquid-phase, mixed-phase and ice clouds, Ph.D. thesis, Johannes Gutenberg-Universität Mainz, https://doi.org/10.25358/openscience-4124, 2018.

Schlenczek, O., Nordsiek, F., Brunner, C. E., Chávez-Medina, V., Thiede, B., Bodenschatz, E., and Bagheri, G.: Airborne measurements of turbulence and cloud microphysics during PaCE 2022 using the Advanced Max Planck CloudKite Instrument (MPCK+), Earth System Science Data Discussions, 2025, 1–29, 2025.

Schröder, M., Bätge, T., Bodenschatz, E., Wilczek, M., and Bagheri, G.: Estimating the turbulent kinetic energy dissipation rate from one-dimensional velocity measurements in time, Atmospheric Measurement Techniques, 17, 627–657, 2024.

Schröder, M.: Cloud Microphysics Investigations with the Cloudkite Laboratory, Ph.D. thesis, Georg-August-Universität Göttingen, https://doi.org/10.53846/goediss-9830, 2023.

Shaw, R. A.: Particle-Turbulence Interactions in Atmospheric Clouds, Annual Review of Fluid Mechanics, 35, 183–227, https://doi.org/10.1146/annurev.fluid.35.101101.161125, 2003.

Siebert, H., Wendisch, M., Conrath, T., Teichmann, U., and Heintzenberg, J.: A new tethered balloon-borne payload for fine-scale observations in the cloudy boundary layer, Boundary-layer meteorology, 106, 461–482, 2003.

Siebert, H., Franke, H., Lehmann, K., Maser, R., Wei Saw, E., Schell, D., Shaw, R. A., and Wendisch, M.: Probing Finescale Dynamics and Microphysics of Clouds with Helicopter-Borne Measurements, Bulletin of the American Meteorological Society, 87, 1727, https://doi.org/10.1175/BAMS-87-12-1727, 2006.

Spuler, S. M. and Fugal, J.: Design of an in-line, digital holographic imaging system for airborne measurement of clouds, Applied Optics, 50, 1405, https://doi.org/10.1364/AO.50.001405, 2011.

Stevens, B., Bony, S., Farrell, D., Ament, F., Blyth, A., Fairall, C., Karstensen, J., Quinn, P. K., Speich, S., Acquistapace, C., Aemisegger, F., Albright, A. L., Bellenger, H., Bodenschatz, E., Caesar, K.-A., Chewitt-Lucas, R., de Boer, G., Delanoë, J., Denby, L., Ewald, F., Fildier, B., Forde, M., George, G., Gross, S., Hagen, M., Hausold, A., Heywood, K. J., Hirsch, L., Jacob, M., Jansen, F., Kinne, S., Klocke, D., Kölling, T., Konow, H., Lothon, M., Mohr, W., Naumann, A. K., Nuijens, L., Olivier, L., Pincus, R., Pöhlker, M., Reverdin, G., Roberts, G., Schnitt, S., Schulz, H., Siebesma, A. P., Stephan, C. C., Sullivan, P., Touzé-Peiffer, L., Vial, J., Vogel, R., Zuidema, P., Alexander, N., Alves, L., Arixi, S., Asmath, H., Bagheri, G., Baier, K., Bailey, A., Baranowski, D., Baron, A., Barrau, S., Barrett, P. A., Batier, F., Behrendt, A., Bendinger, A., Beucher, F., Bigorre, S., Blades, E., Blossey, P., Bock, O., Böing, S., Bosser, P., Bourras, D., Bouruet-Aubertot, P., Bower, K., Branellec, P., Branger, H., Brennek, M., Brewer, A., Brilouet, P.-E., Brügmann, B., Buehler, S. A., Burke, E.,

https://doi.org/10.5194/egusphere-2026-3456
Preprint. Discussion started: 1 July 2026


Burton, R., Calmer, R., Canonici, J.-C., Carton, X., Cato Jr., G., Charles, J. A., Chazette, P., Chen, Y., Chilinski, M. T., Choularton, T., Chuang, P., Clarke, S., Coe, H., Cornet, C., Coutris, P., Couvreux, F., Crewell, S., Cronin, T., Cui, Z., Cuypers, Y., Daley, A., Damerell, G. M., Dauhut, T., Deneke, H., Desbios, J.-P., Dörner, S., Donner, S., Douet, V., Drushka, K., Dütsch, M., Ehrlich, A., Emanuel, K., Emmanouilidis, A., Etienne, J.-C., Etienne-Leblanc, S., Faure, G., Feingold, G., Ferrero, L., Fix, A., Flamant, C., Flatau, P. J., Foltz, G. R., Forster, L., Furtuna, I., Gadian, A., Galewsky, J., Gallagher, M., Gallimore, P., Gaston, C., Gentemann, C., Geyskens, N., Giez, A., Gollop, J., Gouirand, I., Gourbeyre, C., de Graaf, D., de Groot, G. E., Grosz, R., Güttler, J., Gutleben, M., Hall, K., Harris, G., Helfer, K. C., Henze, D., Herbert, C., Holanda, B., Ibanez-Landeta, A., Intrieri, J., Iyer, S., Julien, F., Kalesse, H., Kazil, J., Kellman, A., Kidane, A. T., Kirchner, U., Klingebiel, M., Körner, M., Kremper, L. A., Kretzschmar, J., Krüger, O., Kumala, W., Kurz, A., L'Hégaret, P., Labaste, M., Lachlan-Cope, T., Laing, A., Landschützer, P., Lang, T., Lange, D., Lange, I., Laplace, C., Lavik, G., Laxenaire, R., Le Bihan, C., Leandro, M., Lefevre, N., Lena, M., Lenschow, D., Li, Q., Lloyd, G., Los, S., Losi, N., Lovell, O., Luneau, C., Makuch, P., Malinowski, S., Manta, G., Marinou, E., Marsden, N., Masson, S., Maury, N., Mayer, B., Mayers-Als, M., Mazel, C., McGeary, W., McWilliams, J. C., Mech, M., Mehlmann, M., Meroni, A. N., Mieslinger, T., Minikin, A., Minnett, P., Möller, G., Morfa Avalos, Y., Muller, C., Musat, I., Napoli, A., Neuberger, A., Noisel, C., Noone, D., Nordsiek, F., Nowak, J. L., Oswald, L., Parker, D. J., Peck, C., Person, R., Philippi, M., Plueddemann, A., Pöhlker, C., Pörtge, V., Pöschl, U., Pologne, L., Posyniak, M., Prange, M., Quiñones Meléndez, E., Radtke, J., Ramage, K., Reimann, J., Renault, L., Reus, K., Reyes, A., Ribbe, J., Ringel, M., Ritschel, M., Rocha, C. B., Rochetin, N., Röttenbacher, J., Rollo, C., Royer, H., Sadoulet, P., Saffin, L., Sandiford, S., Sandu, I., Schäfer, M., Schemann, V., Schirmacher, I., Schlenczek, O., Schmidt, J., Schröder, M., Schwarzenboeck, A., Sealy, A., Senff, C. J., Serikov, I., Shohan, S., Siddle, E., Smirnov, A., Späth, F., Spooner, B., Stolla, M. K., Szkółka, W., de Szoeke, S. P., Tarot, S., Tetoni, E., Thompson, E., Thomson, J., Tomassini, L., Totems, J., Ubele, A. A., Villiger, L., von Arx, J., Wagner, T., Walther, A., Webber, B., Wendisch, M., Whitehall, S., Wiltshire, A., Wing, A. A., Wirth, M., Wiskandt, J., Wolf, K., Worbes, L., Wright, E., Wulfmeyer, V., Young, S., Zhang, C., Zhang, D., Ziemen, F., Zinner, T., and Zöger, M.: EUREC$^4$A, Earth System Science Data, 13, 4067–4119, https://doi.org/10.5194/essd-13-4067-2021, 2021.

Stith, J. L., Baumgardner, D., Haggerty, J., Hardesty, R. M., Lee, W.-C., Lenschow, D., Pilewskie, P., Smith, P. L., Steiner, M., and Vömel, H.: 100 Years of Progress in Atmospheric Observing Systems, Meteorological Monographs, 59, 2.1–2.55, https://doi.org/10.1175/AMSMONOGRAPHS-D-18-0006.1, 2018.

Tanaka, T. and Eaton, J. K.: A correction method for measuring turbulence kinetic energy dissipation rate by PIV: Validated by random Oseen vortices synthetic image test, Experiments in fluids, 42, 893–902, 2007.

Thiede, B., Larsen, M. L., Nordsiek, F., Schlenczek, O., Bodenschatz, E., and Bagheri, G.: Highly Localised Droplet Clustering in Shallow Cumulus Clouds, arXiv preprint arXiv:2502.19272, 2025a.

Thiede, B., Nordsiek, F., Kim, Y., Bodenschatz, E., and Bagheri, G.: HoloTrack: In-Situ Holographic Particle Tracking of Cloud Droplets, EGUsphere, 2025, 1–32, 2025b.

Thiede, B., Schlenczek, O., Stieger, K., Ecker, A., Bodenschatz, E., and Bagheri, G.: In-Line Holographic Droplet Imaging: Accelerated Classification with Convolutional Neural Networks and Quantitative Experimental Validation, Manuscript submitted to AMT on 10.02.25, 2025c.

Tropea, C., Yarin, A. L., Foss, J. F., et al.: Springer handbook of experimental fluid mechanics, vol. 1, Springer, 2007.

Verwey, C. and Birouk, M.: Dissipation rate estimation in a highly turbulent isotropic flow using 2D-PIV, Flow, Turbulence and Combustion, 109, 647–665, 2022.

https://doi.org/10.5194/egusphere-2026-3456
Preprint. Discussion started: 1 July 2026


WMO: Guide to Measurements and Methods of Observation, vol. Volume I – Measurement of Meteoroligical Variables of *WMO- No. 8*, World Meteorological Organization, 2018 edition edn., ISBN 978-92-63-10008-5, https://library.wmo.int/index.php?id=12407&lvl=notice_display, 2018.

Zinke, J., Salter, M. E., Leck, C., Lawler, M. J., Porter, G. C., Adams, M. P., Brooks, I. M., Murray, B. J., and Zieger, P.: The development of a miniaturised balloon-borne cloud water sampler and its first deployment in the high Arctic, Tellus, Series B: Chemical and Physical Meteorology, 73, 1–12, https://doi.org/10.1080/16000889.2021.1915614, 2021.